

Effect of the Cassie state in grooved channels on one-dimensional sound wavesAnna Zigelman **Faculty of Mechanical Engineering, Technion–Israel Institute of Technology, Haifa 32000, Israel*Ariella Mansfield *Department of Mechanical Engineering and Applied Mechanics, University of Pennsylvania, Philadelphia, Pennsylvania 19104, USA*Amir D. Gat[†]*Faculty of Mechanical Engineering, Technion–Israel Institute of Technology, Haifa 32000, Israel*

(Received 28 November 2021; accepted 24 May 2022; published 29 June 2022)

Previous experiments and analyses have demonstrated that elastic boundaries reduce the speed of sound and alter the acoustic waves in fluid-filled tubes. Similar effects will occur in any configuration with deformable boundaries and fluid-fluid interfaces. In this work, we study the propagation of nonlinear acoustic waves in 1D liquid-filled tubes with superhydrophobic longitudinal grooved boundaries. Recently, grooved channels have attracted significant interest because of their reduced friction to flow, but such configurations also allow for a new kind of sound wave behavior due to the dependence of the pressure on the triple-phase contact line. We derive a model which contains an interplay between the pressure and the shape of the liquid-gas interface, subject to the hysteresis of the contact line, which is a dominant mechanism for energy dissipation. Our results present front propagation, showing an order of magnitude reduction in the speed of sound, as well as oscillation patterns in which the liquid is pinned in one part of the channel yet oscillating in the rest of the channel.

DOI: [10.1103/PhysRevFluids.7.064803](https://doi.org/10.1103/PhysRevFluids.7.064803)**I. INTRODUCTION**

Previous analyses and experiments demonstrated that elastic walls bounding an internal fluid reduce the speed of acoustic waves propagating in the fluid; see, e.g., [1]. Already in 1847, when Wertheim published experiments measuring the speed of sound of liquids in organ pipes [2], he noticed that the speed of sound was much lower than the previously measured values and attributed this reduction to the cylindrical shape of the liquid (as holds true for solids). Later Helmholtz [3] disproved this theory and noted that the reduction in the speed of sound must depend on pipe wall thickness, elasticity, and diameter. Finally, in 1878, Korteweg [4] found that the speed of propagation of axial acoustic waves in elastic tubes could be expressed by

$$\tilde{c} = \frac{1}{\sqrt{\frac{\rho}{\chi'} + \frac{2r_0\rho}{Eh}}} \quad (1)$$

where \tilde{c} is the speed of sound, $1/\chi'$ is the fluid compressibility, ρ is the fluid density, r_0 is the tube diameter, E is Young's modulus of the pipe's wall, and h is the wall thickness.

*annar@technion.ac.il

†amirgat@technion.ac.il

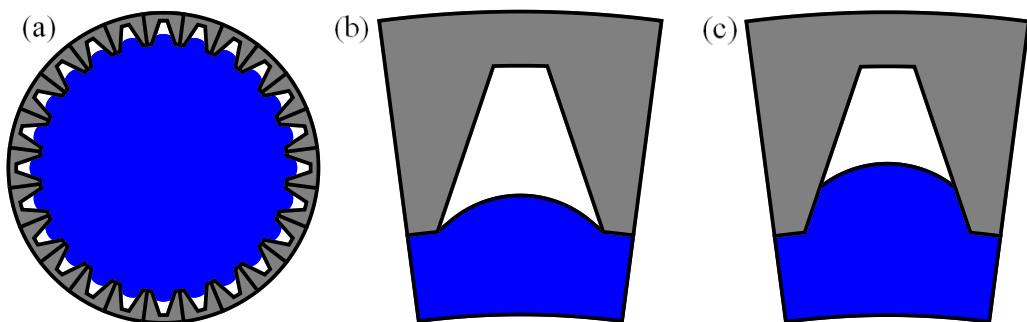


FIG. 1. (a) Cross-sectional view of a slender channel, where the area filled with liquid is colored in blue, and in (b) and (c) two examples of the free surface of the liquid inside the grooves are shown.

In such slender fluid-filled tubes, the elasticity of the boundaries acts to increase the change of mass per length of the channel cross-section fluid due to increased fluidic pressure. This increases the “effective compressibility” of the 1D configuration, thus reducing the axial speed of sound. For the limit of negligible fluid compressibility compared with elastic effects

$$\frac{1}{\chi'} \ll \frac{2r_0}{Eh}, \quad (2)$$

Eq. (1) is reduced to the Moens-Korteweg formula for pulse-wave velocity, commonly used as an indicator of the speed of sound in blood flows [5–9].

In this study we will examine the propagation of sound in channels with Cassie-state walls, wherein gas bubbles become trapped in the vacancies of the microstructure [10]. In particular, the geometry of the grooves in our work (see Fig. 1) was used previously in the literature by Xue *et al.* [11]. There is currently an increasing interest in such channels, which can be used, e.g., for reducing hydrodynamic resistance [12–14] and for other applications [15–18]. Moreover, there exist also numerous theoretical works regarding fluid behavior over such grooved surfaces. For example, Schnitzer [19] considered the effective hydrophobicity of a periodically grooved surface immersed in liquid, with trapped shear-free bubbles protruding between the no-slip ridges at a right contact angle. He derived an asymptotic expansion for the effective slip length and thereby highlighted the (surprisingly) large slip lengths attainable with densely grooved surfaces. Later Schnitzer and Yariv [20] studied the effect of superhydrophobicity where the superhydrophobic surface is formed by a periodically grooved array, in which air bubbles are trapped in a Cassie state, and the solid body is an infinite cylinder. They considered the case where the grooves are aligned perpendicular to the cylinder and allowed for three modes of rigid-body motion: rectilinear motion perpendicular to the surface; rectilinear motion parallel to the surface, in the groove direction; and angular rotation about the cylinder axis. On another note, Schnitzer *et al.* [21] investigated the acoustic response of flat-meniscus bubbles trapped in the grooves of a microstructured hydrophobic substrate immersed in water. They found that bubbles trapped in grooves support multiple subwavelength resonances, which are damped—radiatively—even in the absence of dissipation. Another theoretical study was proposed by Crowdy [22], who presented analytical solutions for longitudinal flow along a superhydrophobic annular pipe where one wall, either the inner or outer, is a fully no-slip boundary while the other is a no-slip wall decorated by a rotationally symmetric pattern of no-shear longitudinal stripes. In particular, he concluded that for a superhydrophobic annular pipe with inner-wall no-shear patterning there is an optimal pipe bore for enhancing hydrodynamic slip for a given pattern of no-shear stripes. Sbragaglia and Prosperetti [23] studied surface deformation on a superhydrophobic surface, where the pressure difference between the liquid and the gas in the grooves causes a curvature of the liquid surface resisted by surface tension. Switching of the two superhydrophobic states, from a Cassie-Baxter state to a Wenzel state, was proposed by Lei *et al.* [24]. This was

achieved by applying pressure to the water in the fluidic chamber, thus leading to the reversible or irreversible change of the diffraction pattern. The irreversible change under high applied pressure was attributed to the switch from Cassie-Baxter state to a Wenzel state. Most recently, Cassie state was studied theoretically, based on 3D Navier-Stokes equations, by Game and coworkers [25], who developed a hybrid asymptotic/numerical method to compute the velocity field through a microchannel textured with periodic longitudinal grooves that support a slowly varying meniscus protrusion and driven by a given pressure drop across the microchannel. In a recent experimental study, Dehe *et al.* [26] demonstrated that by suspending the electrolyte in a Cassie-Baxter state (i.e., employing microstructured superhydrophobic surfaces) the electro-osmotic flow velocity can be increased by an order of magnitude, relatively to no-slip surfaces, thus enabling wider utility of electro-osmotic flow in manipulation of microscale flows.

The configurations studied in the above paragraph naturally involve capillary forces. Such forces interact with interface waves and oscillations, as seen in the review of Perlin and Schultz [27], who discussed the effects of the surface tension on free and forced surface waves for linear, nonlinear, and especially strongly nonlinear waves. To investigate the contact line effects, Miles [28] used a complex-valued boundary condition along the lateral boundaries to allow a phase shift between the free surface and the container boundary. His formulation and solution are analogous to a spring-mass-damper system where the contact line always resists motion, due to capillary hysteresis. Later Henderson and Miles [29] conducted experiments with brimful deep-water conditions in a circular cylinder with clean and with fully contaminated (inextensible) water. They found good agreement between Miles' theory and their increased experimental frequency. The damping rates, however, did not agree, which was attributed to the contact line dynamics (since the contact line was pinned, the contact-line damping was excluded partially in their experiments). Estimates of dissipation at the moving contact line were provided by Milner [30], by assessing the work done by surface tension as the contact-line position and angle change. Using the results of Milner [30], Christiansen *et al.* [31] demonstrated that inclusion of the moving contact line dissipation was required (in addition to the bulk dissipation) to obtain reasonable damping estimates. Confirming these results, by using a large aspect ratio (tank length to width) of 10:1 and deep water, Faraday-wave experiments, and numerical estimates, Jiang [32] found that damping rates were much larger than those predicted by theory without contact-line contributions. Another relevant study was proposed by Gat *et al.* [33], who studied both, theoretically and experimentally, the dynamics of freely moving plates connected by a shallow liquid bridge. They obtained an impulse-like peak in the force applied by the liquid bridge on the plates and linear and nonlinear oscillations of the system for the case of surfaces with low wettability, as a result of small perturbations of the system around the equilibrium point. Most recently, Shelton and Trinh [34] developed an asymptotic theory for steadily traveling gravity-capillary waves under the small-surface tension limit, where it was demonstrated that solutions associated with a perturbation about a leading-order gravity wave (a Stokes wave) contain surface-tension-driven parasitic ripples with an exponentially small amplitude.

Capillary oscillations have many applications. For example, Tan *et al.* [35] studied the interplay between a capillary wave motion and high-frequency surface acoustic waves (SAWs) of a liquid film lying on top of a piezoelectric substrate. Thereafter, Douvidzon *et al.* [36] proposed an experiment for light guided through the water fiber which allows optical interrogation of its capillary oscillations. They further note that coconfining two oscillations in nature, capillary and electromagnetic, might allow a new type of device called microelectrocapillary systems (MECSs). Most recently, Ly and coworkers [37] presented experimental and modeling results of melt pool dynamics, droplet ejections, and hole drilling produced by periodic modulation of laser intensity. The physics of capillary surface wave excitation was discussed and simulation was provided to elucidate the experimental results, which demonstrated that resonant excitation of surface capillary waves can enhance material removal rate by more than $10\times$.

The dynamics of periodic arrays of micrometer-sized liquid-gas menisci formed at superhydrophobic surfaces immersed into water was investigated by Rathgen *et al.* [38], who measured the intensity of optical diffraction peaks in real time. They observed a pronounced resonance at a few

hundred kilohertz. By modeling the system using the unsteady Stokes equation, they concluded that this low resonance frequency was caused by a collective mode of the acoustically coupled oscillating menisci. Later, diffraction patterns of a superhydrophobic surface, consisting of rectangular grooves and which was immersed in water, were used by Rathgen and Mugele [39], enabling them to determine the shape of the menisci and microscopic contact angle.

Since elasticity of the boundaries at the fluid-solid interface affects the speed of sound in slender elastic channels, a similar effect is expected due to surface tension at the liquid-gas interface for open channels. The aim of this work is to relate between capillary oscillations and one-dimensional flows on superhydrophobic grooved surfaces. In particular, we examine the dynamics of waves in superhydrophobic grooved tubes under the effect of capillary waves including the contact line hysteresis, which according to our knowledge was not addressed previously. In Sec. II we present the derivation of the acoustic equation for fluids contained in slender deformable channels. Section III is devoted to the relation between area and pressure in the pinned and unpinned contact line cases, where in addition we show an area-pressure curve during one hysteresis cycle. In Sec. IV we present and discuss our results, and give some concluding remarks in Sec. V.

II. DERIVATION OF THE AXIAL ACOUSTIC EQUATION FOR FLUIDS CONTAINED IN SLENDER CHANNELS WITH DEFORMABLE BOUNDARIES

We examine weak pressure waves propagating in a slender open channel, whose cross section is shown in Fig. 1. The axial direction is x and the cross section lies in the y - z plane. Note that “slender” here means that the the radius of the cross-sectional area is small compared to its length. The compressibility in the model is the compressibility of the liquid, which might be small but not zero.

Similarly to [40] (Chapter 5) integrating the continuity equation over the control volume and applying divergence theorem yields the quasi-1D unsteady mass-conservation and momentum equations [41,42],

$$\frac{\partial}{\partial t}(\rho a) + \frac{\partial}{\partial x}(a \rho u) = 0 \quad (3)$$

and

$$\frac{\partial(\rho u a)}{\partial t} + \frac{\partial(\rho u^2 a)}{\partial x} = -a \frac{\partial p}{\partial x}, \quad (4)$$

where $\rho(x, t)$, $u(x, t)$, and $p(x, t)$ denote the cross-sectionally averaged 1D fluid density, velocity in the x direction, and pressure, respectively, and $a = a(x, t)$ denotes the variable tube’s cross section.

Further, following standard relations for isentropic flow [40], we use the following form of the isentropic relation:

$$\frac{\partial p}{\partial x} = c^2(x, t) \frac{\partial \rho}{\partial x}, \quad (5)$$

where $c(x, t)$ denotes thermodynamic speed of sound.

We define a small parameter, $0 < \epsilon_1 \ll 1$, to be

$$\epsilon_1 := \frac{p_C}{c_0^2 \rho_C}, \quad (6)$$

where $\rho_C := \rho(p = p_{\text{gas}})$ is the density at rest, and p_{gas} is the pressure of gas in the gas-filled area in the groove (for a discussion regarding the pressure of gas in the gas-filled area, see Appendix B), and p_C is the characteristic pressure amplitude. Note that ϵ_1 is a characteristic value of the Mach number.

To render the equations dimensionless we use the following transformations, where the capital letters and ρ_N denote dimensionless quantities. More specifically, we denote the axial coordinate by

X , the speed in x axis by U , the time by T , the cross-sectional area by A , the sound speed by C , and the density by ρ_N , so that

$$X = \frac{x}{l}, \quad U = \frac{u}{\epsilon_1 c_0}, \quad T = \frac{t c_0}{l}, \quad A = \frac{a(p)}{a_C}, \quad C = \frac{c}{c_0}, \quad \rho_N = \frac{\rho}{\rho_C}, \quad (7)$$

where l is the channel length, c_0 is the fluid speed of sound in an unbounded domain, $a_C := a(p = p_{\text{gas}}) = \pi r_i^2$ is the fluid-filled cross-sectional area at the unperturbed pressure p_{gas} , and r_i is the radius of the tube.

Furthermore, we define the normalized fluidic pressure

$$P = \frac{P}{p_{\text{gas}}} = 1 + \frac{P_C}{p_{\text{gas}}} P_1, \quad (8)$$

where P is the scaled pressure and P_1 is the scaled pressure difference from the unperturbed state.

Substituting Eqs. (7) and (8) into (3)–(5), we obtain that the dimensionless system of our equations is given by

$$\frac{\partial}{\partial T}(\rho_N A) + \epsilon_1 \frac{\partial}{\partial X}(A \rho_N U) = 0, \quad (9a)$$

$$\frac{\partial(\rho_N U A)}{\partial T} + \epsilon_1 \frac{\partial(\rho_N U^2 A)}{\partial X} + A \frac{\partial P_1}{\partial X} = 0, \quad (9b)$$

$$\epsilon_1 \frac{\partial P_1}{\partial X} = C^2(X, T) \frac{\partial \rho_N}{\partial X}. \quad (9c)$$

Let us consider the case of small disturbances in the density,

$$\rho_N(X, T) \approx 1 + \epsilon_1 \rho_{N,1}(X, T), \quad (10)$$

and assume that $P_1(X, T)$ is of order $O(1)$ with respect to ϵ_1 . Using (9c), these assumptions imply small disturbances in the speed of sound relative to the speed of sound in the unbounded domain, namely, that

$$C(X, T) \approx 1 + \epsilon_1 C_1(X, T). \quad (11)$$

Similarly, we assume that

$$A(X, T) \approx 1 + K \epsilon_1 A_1[P_1(X, T)], \quad (12)$$

where $K > 0$ is a constant to be discussed in the continuation of this section. The constant K is a degree of freedom which allows us to focus on different timescales, such that in the two limits of K , different mechanisms become more dominant.

Substituting the expansions in Eqs. (10)–(12) into (9), we get at leading order the following system of equations:

$$K A_1' \frac{\partial P_1}{\partial T} + \frac{\partial \rho_{N,1}}{\partial T} + \frac{\partial U}{\partial X} = 0, \quad (13a)$$

$$\frac{\partial P_1}{\partial X} + \frac{\partial U}{\partial T} = 0, \quad (13b)$$

$$\frac{\partial P_1}{\partial X} = \frac{\partial \rho_{N,1}}{\partial X}, \quad (13c)$$

where for brevity we use the following notation: $A_1' := \partial A_1 / \partial P_1$. For further details regarding the derivation of Eq. (13), see Appendix A.

Integrating the isentropic equation, Eq. (13c), with respect to X , we readily get that

$$P_1(X, T) = \rho_{N,1}(X, T), \quad (14)$$

up to a constant of integration.

Differentiating the equation in Eq. (13b) with respect to X yields that

$$\frac{\partial^2 U}{\partial X \partial T} = -\frac{\partial^2 P}{\partial X^2}.$$

Substituting this result and Eqs. (14) into (13a) which was differentiated with respect to T , we get that

$$KA_1'' \left(\frac{\partial P_1}{\partial T} \right)^2 + (1 + KA_1') \frac{\partial^2 P_1}{\partial T^2} - \frac{\partial^2 P_1}{\partial X^2} = 0. \quad (15)$$

The focus of the current study is on the interaction between acoustic waves and the hysteresis of the contact angle. Thus, we shall scale the time so that both effects become of the same order of magnitude. Note that for the limit $0 < K \ll 1$, Eq. (15) degenerates to a standard 1D linear wave equation, which is dominated by fluid compressibility and does not constitute an interesting limit. However, the interesting limit which allows to catch the interplay between acoustic waves and contact angle hysteresis occurs when $K \gg 1$. If the disturbance in area, $A_1[P_1(X, T)]$, is due to the contact angle hysteresis, then based on geometrical considerations which will be explained in Sec. III, it is reasonable to set K to be $K := (h_C \rho_C c_0^2) / (r_i p_C)$, where h_C denotes the characteristic thickness of the fluid inside a groove (between the opening of the groove and the contact line) and r_i is the interior radius of the tube cross section. Note that in the context of the current problem, based on realistic values, we indeed obtained that $K \gg 1$ as desired. To summarize this discussion, note that requesting that the area-dependent terms in Eq. (15) will be of the same order of magnitude as area free terms implies the need to rescale the time appropriately. More specifically, let us rescale the timescale as

$$\tilde{T} = \frac{T}{\sqrt{K}}, \quad (16)$$

which substituted into Eq. (15) yields that

$$A_1'' \left(\frac{\partial P_1}{\partial \tilde{T}} \right)^2 + \left(A_1' + \frac{1}{K} \right) \frac{\partial^2 P_1}{\partial \tilde{T}^2} - \frac{\partial^2 P_1}{\partial X^2} = 0. \quad (17)$$

For brevity, from now on, we shall omit the tilde from T . Note that since $K \gg 1$, the (dimensionless) solution of Eq. (17) is not sensitive to the specific value of K . However, since K affects the timescale according to Eq. (16), the dimensional solution is dependent on K .

An additional assumption which is needed in order to ensure that the contact line motion occurs on the same timescale as the acoustic axial flow, is, as will be stated in Sec. III, that a capillary number is small, $Ca \ll 1$. This in particular implies that the contact line position and the interface equilibrium shape are determined very fast and thus are in equilibrium with the internal pressure. Other limits of the interface dynamics, may also exist, and they should create different wave equations, which are beyond the scope of the current study.

Equation (17) constitutes a nonlinear second-order PDE, where $A_1(P_1)$ is an unknown function. In Sec. III we present geometrical considerations of the Cassie state which enable us to get an algebraic expression for $A_1(P_1)$ in two different cases: a pinned and an unpinned contact line. Afterwards, we explain our approach for the contact angle hysteresis, which is an alternating sequence of pinned and unpinned contact line modes. Then we solve numerically the resulting problem, which is composed of the PDE in Eq. (17) and the equation for the area subject to the contact angle hysteresis for two sets of inset/outset boundary conditions.

III. THE RELATION BETWEEN AREA AND PRESSURE

The effect of surface tension appears only via the function $A_1(P_1)$. In many cases this is not too interesting, due to similarities with known elastic cases. However, surface tension can create

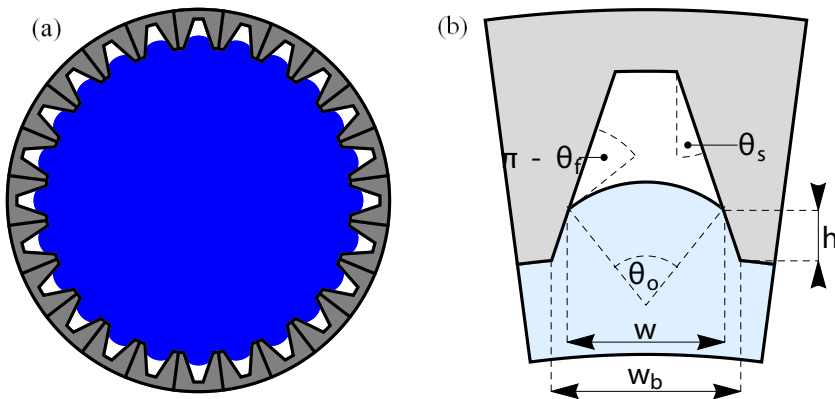


FIG. 2. (a) Cross-sectional view of the channel. (b) An increased view of one groove, where the geometric parameters are indicated.

unexpected results. In this section we present the derivation of the equations only in the hydrophobic case, where the hydrophilic case appears in Appendix C.

A. Hydrophobic case: Geometric considerations and the Young-Laplace relations

Let us assume that the liquid-gas interface is in a quasi steady equilibrium, which is valid when the capillary number is sufficiently small, namely, $Ca = \mu \epsilon_1 \epsilon_2 c_0 / \gamma_f \ll 1$, where γ_f is the surface tension of the free surface, μ is the viscosity of the liquid, and a dimensionless parameter ϵ_2 will be defined in the continuation of this section. This assumption is equivalent to attaining a minimum of surface tension potential energy, and thus the interface cross section can be assumed to be a circular arc (see [43]). Hence, from geometrical considerations the cross-sectional area is given by

$$a(x, t) = \pi r_t^2 + N \left(\frac{r_c^2(x, t)}{2} \{ \theta_o(x, t) - \sin [\theta_o(x, t)] \} + \frac{h(x, t)[w_b + w(x, t)]}{2} \right), \quad (18)$$

where the number of grooves is given by

$$N = \frac{2\pi r_t}{(1 + n_g)w_b}, \quad (19)$$

and where h , w_b , w , θ_o , r_c , and n_g are the distance between the opening of the groove and the contact line, the width of the grooves, the distance between the two contact lines in the grooves, the central angle of the free surface of the liquid, the radius of curvature of the free surface of the liquid, and the ratio distance of grooves (so that $w_b n_g$ is the distance between two adjacent grooves), respectively; see Fig. 2.

This equation is coupled with three additional geometrical relations, which are given in Appendix C, and the following equation which follows from the Young-Laplace equation. More specifically, when neglecting streamwise curvature, we get that the Laplace pressure can be expressed as

$$\frac{\gamma_f}{r_c(x, t)} = p(x, t) - p_{\text{gas}}. \quad (20)$$

Let us define a small parameter, $0 < \epsilon_2 \ll 1$, to be

$$\epsilon_2 := \frac{h_C}{r_t}. \quad (21)$$

Note that the assumption that $0 < \epsilon_2 \ll 1$ means that the area change in each cross section of the tube is very small relatively to the unperturbed area.

We scale the equations in the identical way to the previous section and furthermore define additional dimensionless functions and parameters, as follows:

$$\begin{aligned} H(X, T) &= \frac{h(x, t)}{h_C}, & W(X, T) &= \frac{w(x, t)}{h_C}, \\ R_C(X, T) &= \frac{r_c(x, t)}{h_C}, & R_T &= \frac{\epsilon_2 r_t}{h_C} \equiv 1, & W_b &= \frac{w_b}{h_C}. \end{aligned} \quad (22)$$

Expanding the rescaled area, $A = a/\pi r_t^2$, in asymptotic series in ϵ_2 , namely,

$$A = 1 + \epsilon_2 A_1 [P_1(X, T)], \quad (23)$$

and requesting that the expansion in Eq. (23) coincides with the expansion of A in Eq. (12), we set K to be

$$K := \frac{\epsilon_2}{\epsilon_1} = \frac{h_C \rho_C c_0^2}{r_t \rho_C}. \quad (24)$$

Using standard algebraic manipulations and trigonometric identities, we get that the system of equations in Eqs. (18) and (20) can be expressed as

$$\begin{aligned} A_1(P_1) &= \frac{2}{(1 + n_g)W_b} \left[W_b H(X, T) - H^2(X, T) \tan(\theta_s) \right. \\ &\quad \left. + \frac{1}{2\Pi_c^{-2} P_1^2(X, T)} (2[\theta_f(X, T) - \theta_s] - \pi + \sin\{2[\theta_f(X, T) - \theta_s]\}) \right], \end{aligned} \quad (25a)$$

$$W_b + \frac{2 \cos[\theta_f(X, T) - \theta_s]}{\Pi_c^{-1} P_1(X, T)} = 2H(X, T) \tan(\theta_s), \quad (25b)$$

where θ_s is the inclination angle of the grooves' walls, θ_f is the wetting angle (see Fig. 2), and Π_c denotes the following dimensionless number, which reflects the capillary pressure and is defined as

$$\Pi_c^{-1} := \frac{p_C h_C}{\gamma_f}. \quad (26)$$

For further details see Appendix C.

Hence, for a given pressure, P_1 , we have obtained two equations which are given in Eq. (25) that relate three unknowns: A_1 , H , and θ_f . Thus, in order to solve this system, we need to prescribe an additional unknown among the listed three ones, which is achieved by addressing the pinned and the unpinned contact line cases separately in Secs. III B and III C, respectively. After the discussion regarding the pinned and the unpinned contact line cases, we will discuss in Sec. III D the hysteresis cycle, which is an altering combination of pinned and unpinned contact line modes. In particular, the discussion in Sec. III D should serve as a basis for our numerical algorithm, and thus for the results that are presented in Sec. IV.

B. The pinned case

In the pinned case, H is constant and only the wetting angle changes. Note that Eq. (25b) implies implicitly the following constraint on $\Pi_c^{-1} P_1(X, T)$:

$$|\Pi_c^{-1} P_1(X, T)| \leq \left| \frac{W_b}{2} - H \tan(\theta_s) \right|^{-1}. \quad (27)$$

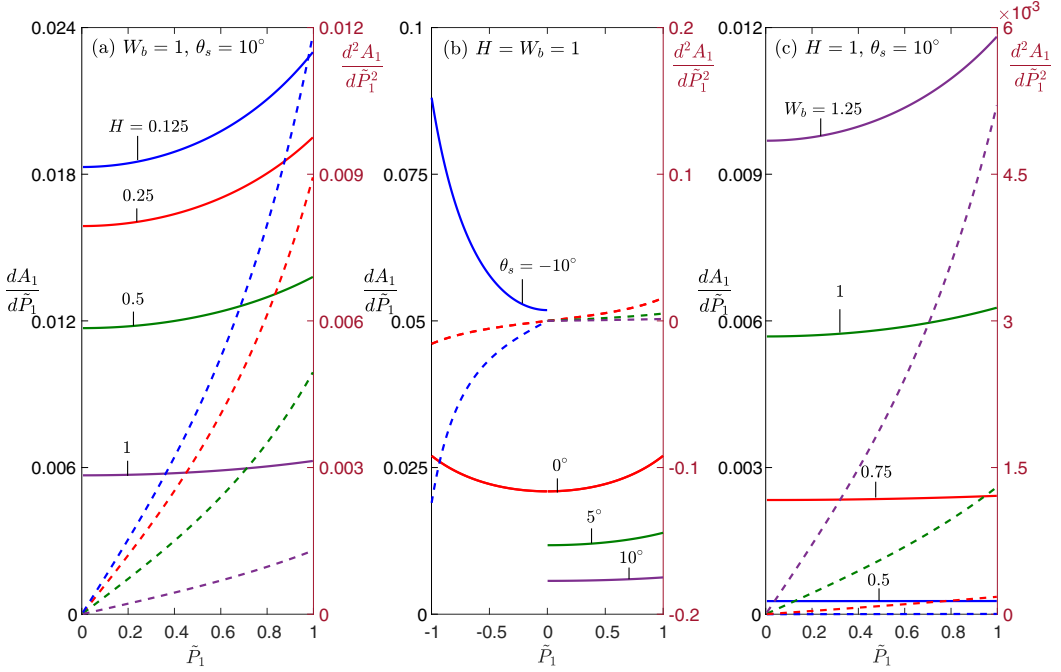


FIG. 3. The plots of the first (shown by solid lines) and the second (shown by the dashed lines of the corresponding color) order derivatives, $dA_1/d\tilde{P}_1$ and $d^2A_1/d\tilde{P}_1^2$, vs $\tilde{P}_1 := \Pi_c^{-1}P_1$ in the pinned contact line case, where $n_g \approx 6.958$ and $h_c = 1$ mm. Further, the parameters in the subplots are as follows: in (a) the different colors stand for different values of H , $H = 0.125, 0.25, 0.5, 1$, and the rest of the parameters are $\theta_s = 10^\circ$ and $W_b = 1$; in (b) the different colors stand for different values of θ_s , $\theta_s = -10^\circ, 0^\circ, 5^\circ, 10^\circ$, and the rest of the parameters are $H = W_b = 1$; in (c) the different colors stand for different values of W_b , $W_b = 0.5, 0.75, 1, 1.25$, and the rest of the parameters are $H = 1$ and $\theta_s = 10^\circ$.

If the constraint in Eq. (27) is satisfied, then Eq. (25b) allows us to isolate θ_f , as follows:

$$\theta_f = \theta_s \pm \arccos \left[\frac{1}{2} [2H \tan(\theta_s) - W_b] \Pi_c^{-1} P_1(X, T) \right]. \quad (28)$$

From geometrical considerations and properties of arcos function, it follows that in the hydrophobic case, where $\theta_s > 0$, P_1 must be nonnegative, and the correct sign in Eq. (28) is plus, so that

$$\theta_f = \theta_s + \arccos \left\{ \frac{1}{2} [2H \tan(\theta_s) - W_b] \Pi_c^{-1} P_1(X, T) \right\}. \quad (29)$$

For further details, see Appendix C.

Substituting Eqs. (29) into (25a), we obtain that

$$\begin{aligned} A_1(P_1) &= \frac{2W_b H - 2H^2 \tan(\theta_s)}{(1 + n_g)W_b} + \frac{1}{(1 + n_g)W_b \Pi_c^{-2} P_1^2} \\ &\times \left[2 \arccos \left\{ \left[H \tan(\theta_s) - \frac{W_b}{2} \right] \Pi_c^{-1} P_1 \right\} - \pi \right. \\ &\left. + \sin \left(2 \arccos \left\{ \left[H \tan(\theta_s) - \frac{W_b}{2} \right] \Pi_c^{-1} P_1 \right\} \right) \right]. \quad (30) \end{aligned}$$

In Fig. 3 we show the dependence of the first (shown by solid lines) and second (shown by dashed lines of the corresponding color) order derivatives, $dA_1/d\tilde{P}_1$ and $d^2A_1/d\tilde{P}_1^2$, on $\tilde{P}_1 := \Pi_c^{-1}P_1$, for $\tilde{P}_1 \in [-1, 1]$ in the pinned contact line case. In Fig. 3(a) we vary H , in Fig. 3(b) we vary the

inclination angle, θ_s , and in Fig. 3(c) we vary the width of each groove, W_b . In all subplots the rest of the parameters are kept fixed.

Note that in the hydrophobic case ($\theta_s > 0$), only a positive range of \tilde{P}_1 is physical, whereas in the hydrophilic case ($\theta_s < 0$), only a negative range of \tilde{P}_1 is physical (see Appendix C 2). For $\theta_s = 0$, both the positive and the negative ranges of \tilde{P}_1 , are physical. It can be seen that in the hydrophobic case the first-order derivative, $dA_1/d\tilde{P}_1$, is a monotone increasing function of \tilde{P}_1 and of W_b and it is a monotone decreasing function of H and of θ_s . In the hydrophilic case, $dA_1/d\tilde{P}_1$ is a monotone decreasing function of \tilde{P}_1 . Moreover, in the case that $\theta_s = 0$ it is a symmetric function with respect to \tilde{P}_1 , which attains a minimum for $\tilde{P}_1 = 0$, it is monotone decreasing for negative values of \tilde{P}_1 and monotone increasing for the positive ones. Moreover, in this case the first-order derivative, $dA_1/d\tilde{P}_1$, is greater in absolute value than the second-order derivative, $d^2A_1/d\tilde{P}_1^2$, by at least a factor of two, reaching in many cases a difference of one order of magnitude or more.

C. The unpinned limit

This limit is even more interesting due to the hysteresis effects. In this limit the wetting angle θ_f is constant (and equal to the receding or advancing value) while H varies, so that Eq. (25a) can be expressed as

$$A_1(P_1) = \frac{1}{(1+n_g)W_b} \left(2W_b H - 2H^2 \tan(\theta_s) + \frac{\{2(\theta_{f,A/R} - \theta_s) - \pi + \sin[2(\theta_{f,A/R} - \theta_s)]\}}{\Pi_c^{-2} P_1^2} \right), \quad (31)$$

where $\theta_{f,A/R}$ denotes either the advancing contact angle value or the receding one. Further, Eq. (25b) can be expressed as

$$H(X, T) = \frac{1}{2 \tan(\theta_s)} \left[W_b + \frac{2 \cos(\theta_{f,A/R} - \theta_s)}{\Pi_c^{-1} P_1(X, T)} \right]. \quad (32)$$

Implicit is here the assumption that since the inclination angle is positive, namely, $\theta_s > 0$, the r.h.s. of Eq. (32) should yield

$$-W_b < \frac{2 \cos(\theta_{f,A/R} - \theta_s)}{\Pi_c^{-1} P_1(X, T)} < 0, \quad (33)$$

which follows from the fact that

$$W = -\frac{2 \cos(\theta_{f,A/R} - \theta_s)}{\Pi_c^{-1} P_1(X, T)},$$

and according to our assumptions W should satisfy $W \in (0, W_b)$. The constraint in Eq. (33) implies that if $0 < (\theta_{f,A/R} - \theta_s) < \pi/2$, then $P_1(X, T)$ must be negative and satisfy

$$\Pi_c^{-1} P_1(X, T) < -\frac{2 \cos(\theta_{f,A/R} - \theta_s)}{W_b}. \quad (34a)$$

Otherwise, if $\pi/2 \leq (\theta_{f,A/R} - \theta_s) < \pi$, then $P_1(X, T)$ must be positive and satisfy

$$\Pi_c^{-1} P_1(X, T) > -\frac{2 \cos(\theta_{f,A/R} - \theta_s)}{W_b}. \quad (34b)$$

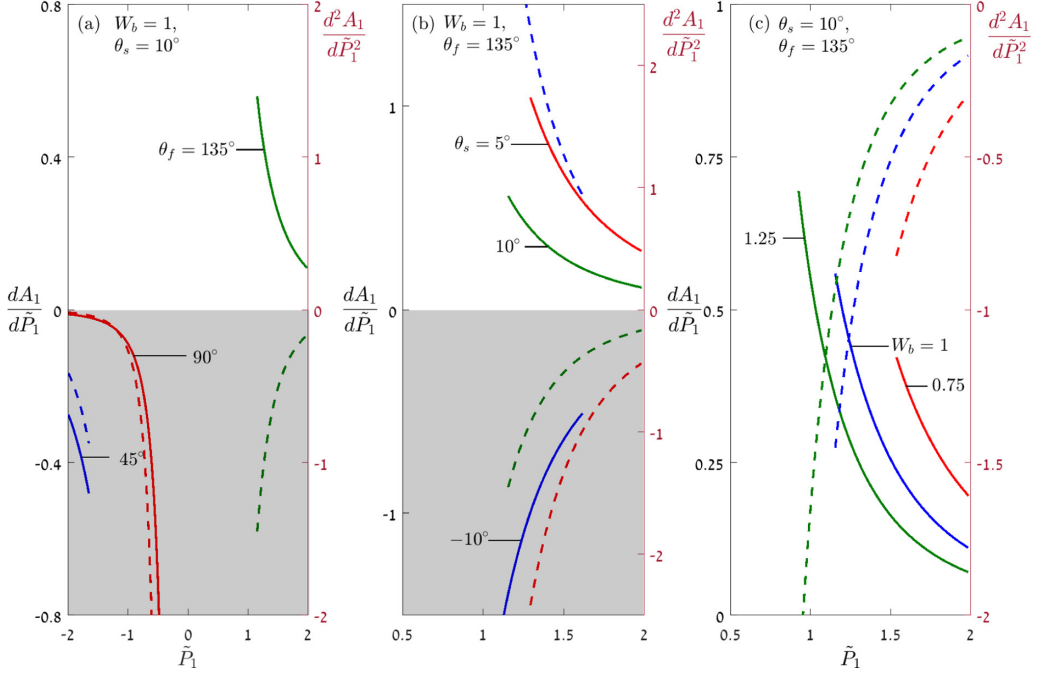


FIG. 4. The first (shown by solid lines) and the second (shown by the dashed lines of the corresponding color) order derivatives, $dA_1/d\tilde{P}_1$ and $d^2A_1/d\tilde{P}_1^2$, vs \tilde{P}_1 in the unpinned contact line case, where $n_g \approx 6.958$ and $h_C = 1$ mm. Further, the parameters in the subplots are as follows: in (a) the different colors stand for different values of the contact angle, θ_f , $\theta_f = 45^\circ, 90^\circ, 135^\circ$, and the rest of the parameters are $\theta_s = 10^\circ$ and $W_b = 1$; in (b) the different colors stand for different values of θ_s , $\theta_s = -10^\circ, 5^\circ, 10^\circ$, and the rest of the parameters are $\theta_f = 135^\circ$ and $W_b = 1$; in (c) the different colors stand for different values of W_b , $W_b = 0.75, 1, 1.25$, and the rest of the parameters are $\theta_s = 10^\circ$ and $\theta_f = 135^\circ$. The gray rectangles represent regions where the solution is unstable (since $dA_1/d\tilde{P}_1 < 0$).

In the case that the constraints in Eq. (34) are satisfied, substituting Eqs. (32) into (31), we conclude that

$$A_1(P_1) = \frac{1}{2(1+n_g)W_b \tan(\theta_s)} \times \left(W_b^2 - \frac{4 \cos^2(\theta_{f,A/R} - \theta_s)}{\Pi_c^{-2} P_1^2} \right) + \frac{\{2(\theta_{f,A/R} - \theta_s) - \pi + \sin[2(\theta_{f,A/R} - \theta_s)]\}}{(1+n_g)W_b \Pi_c^{-2} P_1^2}. \quad (35)$$

In Fig. 4 we show the dependence of the first (shown by solid lines) and second (shown by dashed lines of the corresponding color) order derivatives, $dA_1/d\tilde{P}_1$ and $d^2A_1/d\tilde{P}_1^2$, on $\tilde{P}_1 = \Pi_c^{-1} P_1$, for \tilde{P}_1 in subintervals in $[-2, 2]$ for which the constraints in Eq. (34) [or in Eq. (C18) in the hydrophilic case; see Appendix C 2] are satisfied, in the unpinned contact line case, where the liquid is assumed to be water. In Fig. 4(a) we vary the wetting contact angle of the liquid, θ_f , in Fig. 4(b) we vary the inclination angle, θ_s , and in Fig. 4(c) we vary the width of each groove, W_b . In all subplots the rest of the parameters are kept fixed.

Looking at Fig. 4 it can be seen that the first-order derivative $dA_1/d\tilde{P}_1$ attains maximum at the lowest bound of \tilde{P}_1 , when considering only the range where the constraint holds, and it is a monotone decreasing function of \tilde{P}_1 . When the constraint is not satisfied, this means that the liquid either enters from the groove into the main channel or exits from the main channel into the groove. Moreover, as expected, for $\theta_s = 10^\circ$ only hydrophobic liquids are stable, and vice versa; for the wetting contact

angle of $\theta_f = 135^\circ$ only positive inclinations, $\theta_s > 0$, lead to stable solutions. Furthermore, for $\theta_s = 10^\circ$ and $\theta_f = 135^\circ$ the function $dA_1/d\tilde{P}_1$ is a decreasing function of W_b . Another observation, which differs from the pinned contact line case, is that now the second-order derivative, $dA_1^2/d\tilde{P}_1^2$, is greater in absolute value than the first-order derivative, $dA_1/d\tilde{P}_1$, although both of them are of the same order of magnitude.

D. Hysteresis

Next, let us discuss the hysteresis of the contact line motion and suppose that the pressure, P_1 , is a periodic function of time, where in each period, initially it is a monotone increasing function of time and afterwards a decreasing one. The resulting hysteresis cycle can be described as follows:

(i) Initially, the pressure, P_1 , increases, the liquid contact line is pinned, and the contact angle increases, starting its equilibrium value (which is between the receding and advancing contact angle values), until it reaches the advancing contact angle value.

(ii) When the advancing contact angle is reached, the contact line unpins and starts to move (with a constant contact angle due to a small capillary number; see [43]) towards the grooves' end (to increase the area of the liquid). This continues until the pressure, P_1 , starts to decrease.

(iii) When P_1 starts to decrease, the contact line gets stuck again and the contact angle starts to decrease, in order to reduce the area, until it reaches the receding contact angle value.

(iv) When the receding contact angle is reached, the contact line unpins and starts to slip [with a constant contact angle, similarly to case (ii)] towards the interior of the groove (to decrease the area of the liquid) until the pressure starts to increase again.

The next stage after stage (iv) is stage (i). This cycle repeats, as far as the pressure is a periodic function of time.

We visualize the cycle which was described above by cartoons in Fig. 5, where the solid curves in the graph which were calculated according to Eqs. (30) and (35), show the dependence of the area A_1 on the pressure $\tilde{P}_1 = \Pi_c^{-1}P_1$ in each stage of the dynamics. The liquid was assumed to be water, and the receding and advancing contact angles were assumed to be $\theta_{f,R} = 110^\circ$ and $\theta_{f,A} = 115^\circ$, respectively, and the pinning was assumed to occur for $H = 0.25$ and $H = 1$. The points of intersection of the solid curves indicate what are the critical pressure values for which the interchange from one type of the contact line motion to the the second type occurs. As can be observed, in the pinned contact line cases the area is approximately a linear function of the pressure, \tilde{P}_1 , (and thus of P_1) whereas in the unpinned contact line cases the area is a nonlinear function of \tilde{P}_1 (and thus of P_1) where the nonlinearity is the most evident in the case of the advancing contact angle. Furthermore, it is easy to conclude that the area changes faster in the unpinned regimes of motion than in the pinned ones, and the sharpest change occurs when the interface moves to decrease the wet area with the contact angle which is equal to the receding one.

An additional observation is that, as expected, when looking at the two curves which correspond to the unpinned contact line regimes, the area-pressure curve which corresponds to the advancing contact angle is to the right of the curve, which corresponds to the receding contact angle, because in order to obtain the same area in both cases, more pressure is needed in the cases of a larger wetting contact angle. Moreover, according to the graph, the difference between the pressure needed in order to obtain the same area in the unpinned contact line case with advancing and receding contact angles monotonically increases with increasing the pinning position of the contact line.

IV. RESULTS

In Fig. 6 we show the results of our simulation in Case 1, with sinusoidal signal in the inlet pressure and zero pressure at the outlet, where $\mathcal{A} = 0.4$ and $\omega = 0.5$ (for details regarding the supplementary conditions and the implementation, see Appendix D). More specifically, in Fig. 6(a)

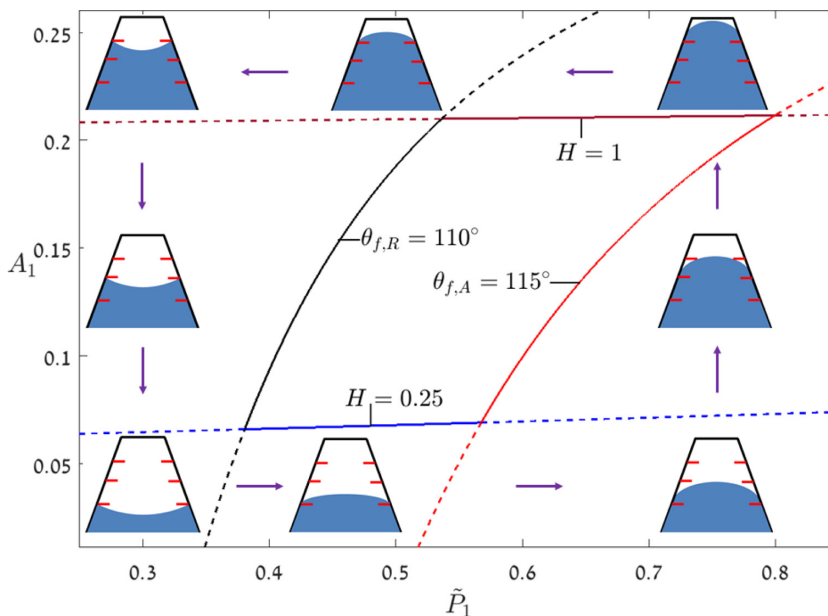


FIG. 5. The solid curves represent area variations as a function of \tilde{P}_1 in a hysteresis cycle, where the red and black curves represent an unpinned contact line motion with constant contact angles, $\theta_{f,A} = 115^\circ$ and $\theta_{f,R} = 110^\circ$, respectively, and blue and maroon curves represent a pinned contact line motion with constant pinning positions, $H = 0.25$ and $H = 1$, respectively. The cartoons and the arrows schematically represent the dynamics of the free surface in one hysteresis cycle which constitutes an increase of the pressure from $\tilde{P}_1 \approx 0.38$ to $\tilde{P}_1 \approx 0.8$, where for $\tilde{P}_1 \approx 0.57$ the evolution changes from pinned contact line motion to the unpinned one, and afterwards the pressure decreases from $\tilde{P}_1 \approx 0.8$ to $\tilde{P}_1 \approx 0.38$, where for $\tilde{P}_1 \approx 0.54$ the evolution changes from pinned contact line motion to the unpinned one. The rest of parameters are $W_b = 1$, $n_g \approx 6.958$, and $\theta_s = 10^\circ$.

we show the temporal variations of the pressure, P_1 , for various positions $X \in (0, 1)$ inside the tube. The pressure waves are seen to be harmonic. As can be seen, the sinusoidal (in T) oscillations are with an amplitude which depends on X but is independent of T and as we move towards $X = 1$ the oscillations decay. In Figs. 6(b) and 6(d) we show the temporal variations of the contact angle, θ_f , and the corresponding film thickness, H , for various positions $X \in (0, 1)$ inside the tube. Note that we obtained square waves for the position of the contact line. Moreover, it can be observed that only in a part of the tube a full hysteresis cycle occurs, whereas in the rest of the tube the contact line is pinned. The transition between the hysteresis and the pinned contact line regime occurs for some X in the range $X \in (0.2, 0.4)$, where the height of the contact line, H , in the pinned contact line region decreases as we move from $X = 0$ to $X = 1$. Furthermore, the hysteresis cycles decrease, in the sense that the distance between the two pinned positions decreases, as we move from $X = 0$ towards the tube interior, until the hysteresis disappears at all and interchanges to a pinned regime. This fact is also visualized in Fig. 6(c), where we show the dependence of pressure, P_1 , on the area, A_1 . In this panel, it can be seen that after an initial transient, either the system enters into a hysteresis mode, where the cycles get smaller and smaller as we move toward the interior of the tube, or it oscillates on the same path where the pressure variations and the area decrease as we move toward $X = 1$. See the corresponding movie in the Supplemental Material [44], representing the temporal evolution of the pressure, P_1 , film thickness, H , and contact angle, θ_f as a function of X , for $T \in (0, 60]$.

In Fig. 7 we show the results of our simulation in Case 2, with a sudden increase in the inlet pressure and no flux boundary conditions in the outlet, where $\mathcal{B} = 0.5$ (for details regarding the

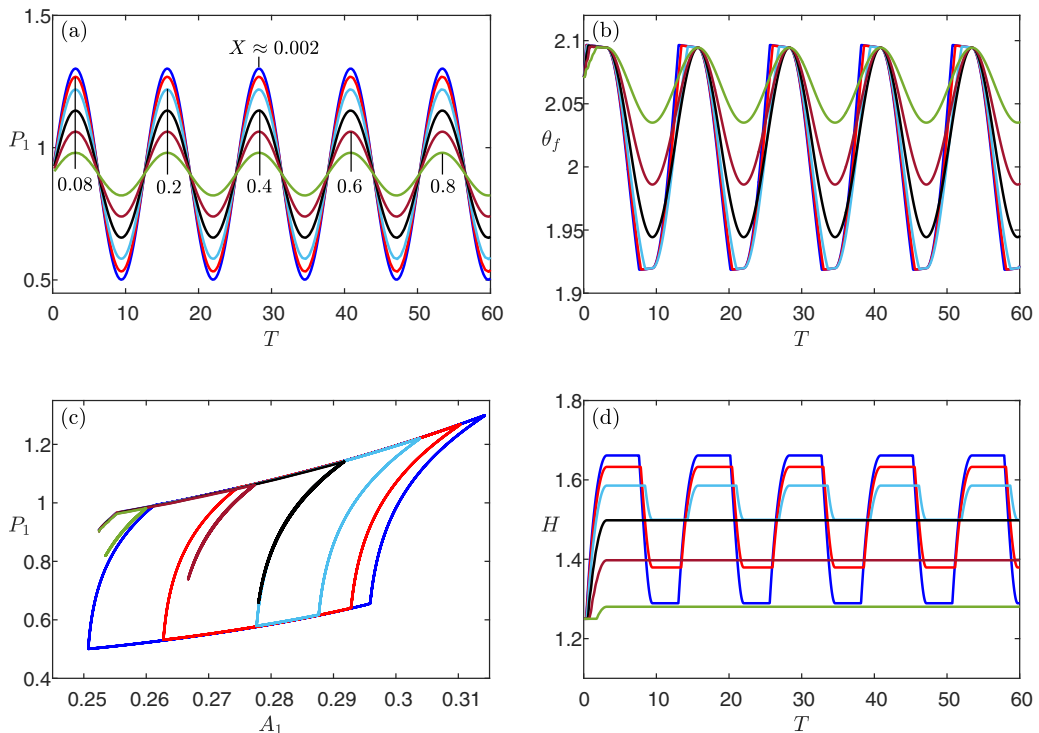


FIG. 6. Periodic evolution of the pressure inside the tube in Case 1, where $W_b = 1$, $n_g \approx 6.958$, $\theta_s = 10^\circ$, $\theta_{f,R} = 110^\circ$, $\theta_{f,A} = 120^\circ$, and the amplitude and the frequency satisfy $\mathcal{A} = 0.4$ and $\omega = 0.5$, respectively, where in (a) we show temporal, T , variations of the pressure, P_1 , in (b) temporal variations of the contact angle, θ_f , in (c) the dependence of the pressure, P_1 , on the area of the corresponding cross section, A_1 , and in (d) temporal variations of the height of the film, H . The colors of the curves indicate different positions, $X \in (0, 1)$, of the corresponding cross sections inside the tube. See the corresponding movie in the Supplemental Material [44].

supplementary conditions and the implementation, see Appendix D). More specifically, in Fig. 7(a) we show the temporal variations of the pressure, P_1 , for various positions $X \in (0, 1)$ inside the tube. In this case, after an initial transient, we get slowly decaying oscillations in the pressure. Furthermore, the amplitude of the oscillations increases as we move towards $X = 1$. This oscillatory behavior is a consequence of incorporating the area variations into the equation; without taking this into account in the model the pressure would tend to a steady state which would be achieved after an initial transient. The oscillatory behavior of the current case is also visualized in Fig. 7(b), where we show the dependence of the pressure, P_1 , on the area, A_1 . As can be observed, after an initial transient (during which the point near the outlet manages to perform a hysteresis cycle), the system enters into some path, whose length increases as we move toward $X = 1$. After entering the corresponding path, the system starts to oscillate along it as time moves on. In Figs. 7(b) and 7(c) we show the temporal variations of the contact angle, θ_f , and the corresponding film thickness, H . In particular, these panels indicate that inside the tube only the pinned contact regime holds, where as we move toward $X = 1$, the film thickness increases and the amplitude of the oscillations in θ_f increases as well. See the corresponding movie in the Supplemental Material [44], representing the temporal evolution of the pressure, P_1 , film thickness, H , and contact angle, θ_f as a function of X , for $T \in (0, 7]$.

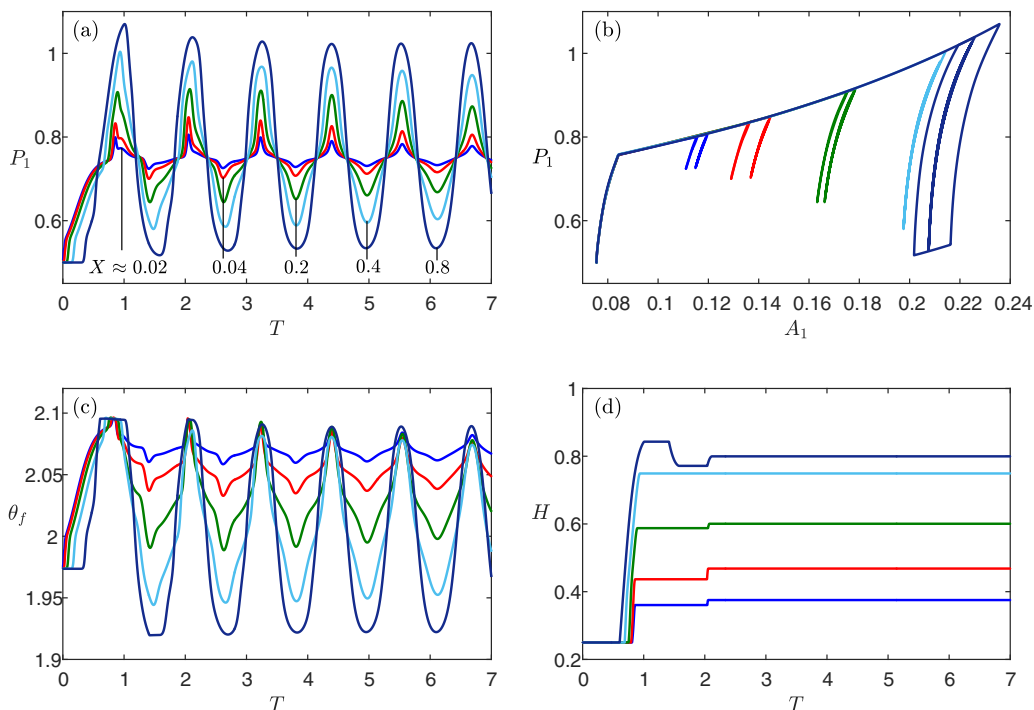


FIG. 7. Periodic evolution of the pressure inside the tube in Case 2, where $W_b = 0.8$, $n_g \approx 5.4$, $\theta_s = 10^\circ$, $\theta_{f,R} = 110^\circ$, $\theta_{f,A} = 120^\circ$, and the prefactor of the Heaviside function is given by $\mathcal{B} = 0.5$, where in (a) we show temporal, T , variations of the pressure, P_1 , in (b) the dependence of the pressure, P_1 , on the area of the corresponding cross section, A_1 , in (c) temporal variations of the contact angle, θ_f , and in (d) temporal variations of the height of the film, H . The colors of the curves indicate different positions, $X \in (0, 1)$, of the corresponding cross sections inside the tube. See the corresponding movie in the Supplemental Material [44].

In Figs. 8(a) and 8(b) we show spatial variations of the pressure P_1 and the contact angle, θ_f , at early times, $T \in (0, 0.5)$, and in Figs. 8(c) and 8(d) we show spatial variations of the pressure P_1 and the contact angle, θ_f , during one representative cycle, for $T \in [1.84, 3]$, which takes place after the initial transient. Looking at Figs. 8(a) and 8(b) it can be seen that the pressure front propagates inside the tube, from the inlet till the outlet, which is reflected by the increase in the contact angle. Note that in this example after about $T = 0.35$ the front reaches the outlet. If we transform T to dimensional time (see discussion in Sec. II), where we assume that the liquid is water, so that $c_0 = 1000$ m/s and $\rho_C = 1000$ kg/m³, and the characteristic length and tube's radius are $l = 1$ m and $r_t = 10^{-4}$ m, respectively, and use the scaling for pressure $p_C \approx 1271$ Pa we get that it takes about

$$t = 0.35 \times l \frac{\sqrt{K}}{c_0} \approx 0.031 \text{ sec}$$

for the signal to reach the outlet. This means that the speed of pressure front propagation under the current conditions (with the hysteresis effect) is equal approximately to $1/0.031 \approx 32$ m/sec, which is about 30 times slower than the speed of sound. For an additional example of gradual propagation of the pressure signal, which is reflected by the corresponding propagation of the increase in the film thickness (unpinned case) with sinusoidal signal in the inlet as in Case 1, but with a much larger frequency of $\omega = 10$, see the corresponding movie in the Supplemental Material [44].

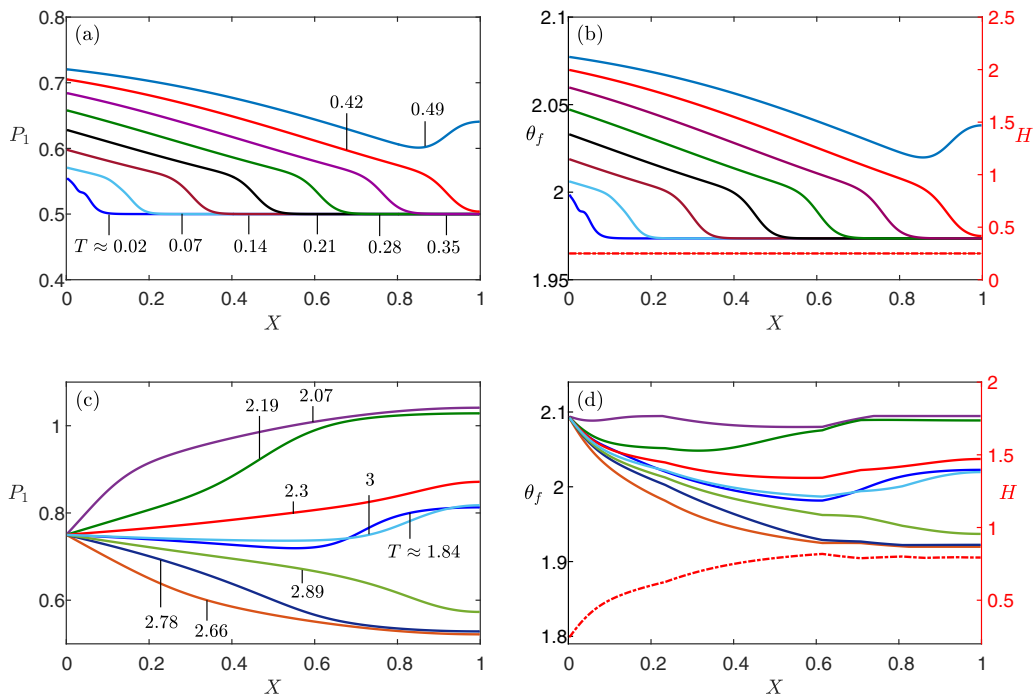


FIG. 8. (a), (b) Spatial, X , variations of the pressure, P_1 , and the contact angle, θ_f , respectively, at early times $T \in [0.02, 0.49]$ (just after inserting pressure in the inlet). (c), (d) Spatial, X , variations of the pressure, P_1 , and the contact angle, θ_f , respectively, at a representative cycle (where the film thickness, H , has already reached a steady state), for $T \in [1.84, 3]$. The different colors in (a) and (b) as well as in (c) and (d) correspond. In (b) and (d) the film thickness H is marked by a dotted-dashed red line, and the dashed blue lines in (c) and (d) emphasize that at the end of the cycle P_1 and θ_f almost coincide with the corresponding functions at the beginning of the cycle.

After the signal reaches the outlet, the pressure starts to oscillate, where during the first period the contact angle increases up to the advancing value, $\theta_{f,A}$, which is followed by the unpinned mode of motion during which the liquid-air interface reaches a steady-state thickness, H [shown in Fig. 8(d) by a dotted-dashed line]. In all of the next cycles, the pressure, P_1 , and the contact angle, θ_f , oscillate together, as can be seen in Figs. 8(c) and 8(d). Note that the curves of $P_1(X, T = 1.84)$ and $P_1(X, T = 3)$, obtained approximately at the beginning and at the end of a cycle, respectively, are very close, and so are the corresponding curves of the contact angles, $\theta_f(X, T = 1.84)$ and $\theta_f(X, T = 3)$. Thus, the wavelength is about $\Delta T \approx 1.16$, which transformed to the dimensional variables yields the wavelength of $\Delta t \approx 0.1$ sec. An additional observation is that the pressure curves, $P_1(X, T)$, are not symmetric as a function of T around $P_1 = 0.7$; this nonsymmetric behavior can be also observed in Fig. 7(a).

V. CONCLUSIONS

In this study, we investigated the effects of contact angle hysteresis on the propagation of sound waves in a long channel with Cassie state boundaries. The model that we propose consists of a coupled system of a nonlinear PDE for the pressure propagation which is affected by the first- and second-order derivatives of the area relative to the pressure and an algebraic nonlinear equation for the area dependence on the pressure, under the assumption of negligible viscous effects. Our numerical approach enabled us to solve this coupled system under the assumption of contact

angle hysteresis, which is the dominant cause for energy dissipation when viscous effects may be neglected.

Our model enables us to estimate the speed of signal propagation, which depends on a dimensionless number \sqrt{K} ; see Sec. II. For example, in this study we portrayed the behavior of waves which propagate in the tube filled with water approximately 30 times slower than the speed of sound in water. In the case of sinusoidal wave in the inlet, we obtained harmonic waves for the pressure, and square waves for the location of the contact line. In the case of a Heaviside signal in the inlet we obtained an initially propagating pressure front and later slowly decaying oscillations. Moreover, our results indicate that the hysteresis occurs only in a part of the channel, where in the rest of it the contact line is pinned, and the pressure oscillates together with the contact angle (which is always between its advancing and receding values). Sometimes (as in Fig. 6) the hysteresis (in a part of the channel) occurs during the whole simulation time in which case in a part of the channel the liquid height, H , is fixed and the other part of the contact line oscillates during the whole simulation period, where sharp angles may form between the two (steady and moving) parts of the contact line. See movies in the Supplemental Material [44]. In other cases (as in Figs. 7 and 8) the hysteresis (in a part of the channel) occurs only during an initial transient, and after this transient period, the contact line remains in a nonuniform steady state throughout the tube. This behavior will eventually lead to a steady state with constant pressure, but nonuniform values of contact line height and contact angle, which depend on spatial position along the tube.

To conclude, in this interaction between acoustics and the triple-phase contact line, as well as the hysteresis of the wetting angle, highly nonlinear acoustic equations emerge, which are not described in previous literature to our best knowledge. The equations, together with their derivation and wave solutions, constitute a unique kind of wave, where hysteresis of the contact line facilitates significant and unusual energy dissipation. While the present study is motivated by academic interests, these waves may also be used in practical applications, for instance, as a way to filter acoustic noises of specific amplitudes or frequencies, or to assess a Cassie state through acoustics.

The authors report no conflict of interest.

APPENDIX A: DERIVATION OF THE GOVERNING LEADING ORDER SYSTEM

In this section we shall present our derivation of Eqs. (13). Let us start our discussion from Eq. (9a). Substituting the expansions in Eqs. (10) and (12) into Eq. (9a), we get that

$$\epsilon_1 \left\{ (1 + K\epsilon_1 A_1) \frac{\partial \rho_{N,1}}{\partial T} + K(1 + \epsilon_1 \rho_{N,1}) \frac{\partial A_1}{\partial T} + \frac{\partial}{\partial X} [(1 + K\epsilon_1 A_1)(1 + \epsilon_1 \rho_{N,1})U] \right\} = 0. \quad (\text{A1})$$

Now, dividing by ϵ_1 and using the chain rule for $A_1[P_1(X, T)]$, we obtain at leading order Eq. (13a).

Next, let us consider Eq. (9b). First, note that

$$\frac{\partial(\rho_N U A)}{\partial T} = U \frac{\partial(\rho_N A)}{\partial T} + \rho_N A \frac{\partial U}{\partial T},$$

so that by Eq. (9a), it follows that

$$\frac{\partial(\rho_N U A)}{\partial T} = -\epsilon_1 U \frac{\partial}{\partial X} (A \rho_N U) + \rho_N A \frac{\partial U}{\partial T}.$$

Substituting this into Eq. (9b), we get that

$$-\epsilon_1 U \frac{\partial}{\partial X} (A \rho_N U) + \rho_N A \frac{\partial U}{\partial T} + \epsilon_1 \frac{\partial(\rho_N U^2 A)}{\partial X} + A \frac{\partial P_1}{\partial X} = 0. \quad (\text{A2})$$

Thus, substituting the expansions in Eqs. (10) and (12) into (A2), we obtain at leading, $O(1)$ order with respect to ϵ_1 , that

$$\frac{\partial U}{\partial T} + \frac{\partial P_1}{\partial X} = 0, \quad (\text{A3})$$

exactly as it was stated in Eq. (9b).

Derivation of Eq. (9c) is trivial.

APPENDIX B: DISCUSSION ON THE PRESSURE OF THE GAS IN THE GROOVES

Our model assumes constant atmospheric pressure at the gas phase. This does not require specifically that the compressibility of the gas is negligible, but rather that the timescale in which the gas reaches equilibrium is much smaller than that of acoustic waves. Since the gas is open to atmospheric pressure at both the inlet and outlet, equilibrium means constant atmospheric pressure, as assumed in this study. Nonetheless, we can write a condition allowing us to neglect pressure changes in the gas, even without reaching equilibrium (flow of the gas to the surroundings via the vertical grooves). For this strict lower limit, the change in capillary pressure within the wave cycle needs to be of order of magnitude greater than the change in the pressure within the gas for exactly the same cycle. In other words, the requirement which allows us to neglect the pressure changes in the gas in dimensional notation is as

$$\frac{\partial a_1}{\partial p_1} \ll \frac{\partial a_1}{\partial p_{\text{gas}}}, \quad (\text{B1})$$

where p_1 and a_1 denote the first-order corrections for the pressure and area of the liquid, and p_{gas} is the pressure of gas in the gas-filled area in the groove. Now, since according to the ideal gas law,

$$p_{\text{gas}} = \frac{N\tilde{m}_{\text{gas}}R\mathcal{T}}{(a_{0,\text{gas}} - a_1)},$$

where \tilde{m}_{gas} denotes the gas mass per unit length in x direction, N is the number of grooves, $a_{0,\text{gas}}$ denotes the combined unperturbed area of the gas phase in the grooves, R is the ideal gas constant, and \mathcal{T} is temperature, we get that

$$a_1 = a_{0,\text{gas}} - \frac{N\tilde{m}_{\text{gas}}R\mathcal{T}}{p_{\text{gas}}},$$

which implies that

$$\frac{\partial a_1}{\partial p_{\text{gas}}} = \frac{N\tilde{m}_{\text{gas}}R\mathcal{T}}{p_{\text{gas}}^2} = \frac{a_{0,\text{gas}} - a_1}{p_{\text{gas}}}. \quad (\text{B2})$$

In order to satisfy Eq. (B1) we need to compare the value obtained from Eq. (B2) with the gradients appearing within the cycle, as shown in Fig. 5. Scaling arguments immediately give a simple requirement of $a_1 \ll a_{0,\text{gas}}$.

APPENDIX C: DERIVATION OF THE DEPENDENCE OF AREA ON PRESSURE

1. Hydrophobic case

Equation (18) is coupled with the following equations, which follow from geometric relations. First, since the cross section of the liquid constitutes an arc of a circle inside each groove, we obtain the following relation between the opening angle of the cross section of the liquid, $\theta_o(x, t)$, its radius of curvature, $r_c(x, t)$, and the distance between the two contact lines inside the groove or

equivalently the distance between the two ends of the arc, $w(x, t)$,

$$\sin\left(\frac{\theta_o(x, t)}{2}\right) = \frac{w(x, t)}{2r_c(x, t)}. \quad (\text{C1})$$

Next, since as it possible to observe, the complementary angle of the contact angle, $\pi - \theta_f$, half the opening angle, $\theta_o(x, t)/2$, and the inclination angle of the groove wall, $\theta_s > 0$, sum up to a right angle, which leads to

$$\frac{\pi}{2} + \frac{\theta_o(x, t)}{2} + \theta_s = \theta_f(x, t). \quad (\text{C2})$$

Moreover, as it is easy to verify, the distance between the two contact lines inside the groove, $w(x, t)$, is related to the opening length of the groove, w_b , the thickness of the liquid inside the groove, $h(x, t)$, and the inclination angle of the groove wall, θ_s , as follows:

$$w(x, t) = w_b - 2h(x, t) \tan(\theta_s). \quad (\text{C3})$$

Substituting the scaling in Eq. (7) and Eq. (22) into the system in Eqs. (18), (20), and (C1)–(C3), we get the following dimensionless system of equations:

$$A(X, T) = \frac{h_c^2}{r_t^2} \left(\epsilon_2^{-2} + \frac{\epsilon_2^{-1}}{(1+n_g)W_b} \{R_C^2(X, T)\{\theta_o(X, T) - \sin[\theta_o(X, T)]\} + H(X, T)[W_b + W(X, T)]\} \right), \quad (\text{C4a})$$

$$\sin\left(\frac{\theta_o(X, T)}{2}\right) = \frac{W(X, T)}{2R_C(X, T)}, \quad (\text{C4b})$$

$$\frac{\pi}{2} + \frac{\theta_o(X, T)}{2} + \theta_s = \theta_f(X, T), \quad (\text{C4c})$$

$$W(X, T) = W_b - 2H(X, T) \tan(\theta_s), \quad (\text{C4d})$$

$$P_1(X, T) = \frac{\gamma_f}{\rho_C h_C R_C(X, T)}. \quad (\text{C4e})$$

Next, substituting the expansions in Eqs. (23) into (C4), we get that

$$1 + \epsilon_2 A_1(P_1) = \frac{h_c^2}{r_t^2} \left\{ \epsilon_2^{-2} + \frac{\epsilon_2^{-1}}{(1+n_g)W_b} (R_C^2(X, T)\{\theta_o(X, T) - \sin[\theta_o(X, T)]\} + H(X, T)[W_b + W(X, T)]) \right\}, \quad (\text{C5a})$$

$$\sin\left(\frac{\theta_o(X, T)}{2}\right) = \frac{W(X, T)}{2R_C(X, T)}, \quad (\text{C5b})$$

$$\frac{\pi}{2} + \frac{\theta_o(X, T)}{2} + \theta_s = \theta_f(X, T), \quad (\text{C5c})$$

$$W(X, T) = W_b - 2H(X, T) \tan(\theta_s), \quad (\text{C5d})$$

$$P_1(X, T) = \frac{\gamma_f}{\rho_C h_C R_C(X, T)}. \quad (\text{C5e})$$

Then, using $W(X, T)$ which is given in Eq. (C5d) and θ_0 which according to Eq. (C5c) can be expressed as

$$\theta_o(X, T) = 2(\theta_f(X, T) - \theta_s) - \pi, \quad (\text{C6})$$

we get that

$$1 + \epsilon_2 A_1(P_1) = \frac{h_C^2}{r_t^2} \left\{ \epsilon_2^{-2} + \frac{\epsilon_2^{-1}}{(1+n_g)W_b} [2W_b H(X, T) - 2H^2(X, T) \tan(\theta_s) + R_C^2(X, T)] \right. \\ \left. \times [2[\theta_f(X, T) - \theta_s] - \pi + \sin\{2[\theta_f(X, T) - \theta_s]\}] \right\}, \quad (C7a)$$

$$W_b + 2R_C(X, T) \cos[\theta_f(X, T) - \theta_s] = 2H(X, T) \tan(\theta_s), \quad (C7b)$$

$$P_1(X, T) = \frac{\gamma_f}{p_c h_C R_C(X, T)}, \quad (C7c)$$

where we have used basic trigonometric identities, such as

$$\sin(\alpha - \pi) = -\sin(\alpha) \quad \text{and} \quad \sin(\alpha - \pi/2) = -\cos(\alpha),$$

which are valid for any angle α .

Now, using Eq. (C7c), we find that R_C can be expressed as

$$R_C(X, T) = \frac{\gamma_f}{p_c h_C P_1(X, T)}. \quad (C8)$$

Substituting this into Eqs. (C7a)–Eq. (C7b), we get that

$$1 + \epsilon_2 A_1(P_1) = \frac{h_C^2}{r_t^2} \left\{ \epsilon_2^{-2} + \frac{\epsilon_2^{-1}}{(1+n_g)W_b} \left[2W_b H(X, T) - 2H^2(X, T) \tan(\theta_s) \right. \right. \\ \left. \left. + \frac{\gamma_f^2 (2[\theta_f(X, T) - \theta_s] - \pi + \sin\{2[\theta_f(X, T) - \theta_s]\})}{[p_c h_C P_1(X, T)]^2} \right] \right\}, \quad (C9a)$$

$$W_b + \frac{2\gamma_f \cos(\theta_f(X, T) - \theta_s)}{h_C p_c h_C P_1(X, T)} = 2H(X, T) \tan(\theta_s). \quad (C9b)$$

Next we recall the definition of ϵ_2 , by which it follows that

$$h_C = \epsilon_2 r_t,$$

whose substitution into Eq. (C9) leads to

$$1 + \epsilon_2 A_1(P_1) = 1 + \frac{\epsilon_2}{(1+n_g)W_b} \left[2W_b H(X, T) - 2H^2(X, T) \tan(\theta_s) \right. \\ \left. + \frac{\gamma_f^2 (2[\theta_f(X, T) - \theta_s] - \pi + \sin\{2[\theta_f(X, T) - \theta_s]\})}{[p_c h_C P_1(X, T)]^2} \right], \quad (C10a)$$

$$W_b + \frac{2\gamma_f \cos[\theta_f(X, T) - \theta_s]}{p_c h_C P_1(X, T)} = 2H(X, T) \tan(\theta_s), \quad (C10b)$$

which leads to the expression in Eq. (25), where the dimensionless number Π_c^{-1} was defined in Eq. (26).

In the pinned contact line case, we need to decide what is the correct sign in the expression in Eq. (28). Based on Eq. (27), if $P_1 \geq 0$, we may easily conclude that

$$\pi/2 = \arccos(0) \leq \arccos\left(\frac{1}{2}[2H \tan(\theta_s) - W_b]\Pi_c^{-1}P_1\right) \leq \arccos(-1) = \pi. \quad (\text{C11})$$

However, according to Eq. (C4c), θ_f should satisfy

$$\theta_f = \theta_s + \frac{\pi}{2} + \frac{\theta_o(X, T)}{2}, \quad (\text{C12})$$

where it is obvious that $\theta_o(X, T) \geq 0$, and thus $\pi/2 + \theta_o(X, T)/2 > 0$. Hence, when looking on Eq. (28), we may conclude that only the positive root in Eq. (28) is the physical solution in our case, which yields Eq. (29). To justify that P_1 must be nonnegative when $\theta_s > 0$, let us assume for a moment that $P_1 < 0$. This assumption implies, instead of Eq. (C11), that

$$0 = \arccos(1) \leq \arccos\left\{\frac{1}{2}[2H \tan(\theta_s) - W_b]\Pi_c^{-1}P_1\right\} \leq \arccos(0) = \pi/2, \quad (\text{C13})$$

so that Eq. (C12) cannot hold for both choices of sign in Eq. (28).

2. Hydrophilic case: Geometric considerations and the Young-Laplace relations

Note that the assumption that the capillary number is small, $\text{Ca} \ll 1$, remains valid also in this case. Now we assume that in this case the groove has an opposite orientation, which means that $\theta_s < 0$. From geometrical considerations, the curvature is negative in this case, namely, $r_c < 0$, and the equations now become

$$a(x, t) = \pi r_t^2 + N \left(-\frac{r_c^2(x, t)}{2} \{\theta_o(x, t) - \sin[\theta_o(x, t)]\} + \frac{h(x, t)[w_b + w(x, t)]}{2} \right), \quad (\text{C14a})$$

$$\sin\left(\frac{\theta_o(x, t)}{2}\right) = -\frac{w(x, t)}{2r_c(x, t)}, \quad (\text{C14b})$$

$$\frac{\pi}{2} - \frac{\theta_o(x, t)}{2} + \theta_s = \theta_f(x, t), \quad (\text{C14c})$$

$$w(x, t) = w_b - 2h(x, t) \tan(\theta_s), \quad (\text{C14d})$$

$$\frac{\gamma_f}{r_c(x, t)} = p(x, t) - p_{\text{gas}}. \quad (\text{C14e})$$

Substituting the scaling in Eqs. (7) and (22) into the system in Eq. (C14), we get the following dimensionless system of equations:

$$A(X, T) = \frac{h_C^2}{r_t^2} \left(\epsilon_2^{-2} + \frac{\epsilon_2^{-1}}{(1+n_g)W_b} \{-R_C^2(X, T)\{\theta_o(X, T) - \sin[\theta_o(X, T)]\} + H(X, T)[W_b + W(X, T)]\} \right), \quad (\text{C15a})$$

$$\sin\left(\frac{\theta_o(X, T)}{2}\right) = -\frac{W(X, T)}{2R_C(X, T)}, \quad (\text{C15b})$$

$$\frac{\pi}{2} - \frac{\theta_o(X, T)}{2} + \theta_s = \theta_f(X, T), \quad (\text{C15c})$$

$$W(X, T) = W_b - 2H(X, T) \tan(\theta_s), \quad (\text{C15d})$$

$$P_1(X, T) = \frac{\gamma_f}{p_C h_C R_C(X, T)}. \quad (\text{C15e})$$

Substituting the expansion in Eq. (23), isolating $W(X, T)$, $\theta_o(X, T)$, and $R_C(X, T)$, as well as using the definition of ϵ_2 which was prescribed in Eq. (21), we get that our system of equations can be expressed as

$$A_1(P_1) = \frac{2}{(1+n_g)W_b} \{W_b H(X, T) - H^2(X, T) \tan(\theta_s)\} + \frac{1}{2\Pi_c^{-2}P_1^2(X, T)} (2[\theta_f(X, T) - \theta_s] - \pi + \sin\{2[\theta_f(X, T) - \theta_s]\}), \quad (\text{C16a})$$

$$W_b + \frac{2 \cos p\theta_f(X, T) - \theta_s}{\Pi_c^{-1}P_1(X, T)} = 2H(X, T) \tan(\theta_s), \quad (\text{C16b})$$

exactly as it was in the hydrophobic case.

In the pinned contact line case, under the assumption in Eq. (27), we get now that

$$\theta_f = \theta_s + \arccos\left(\frac{1}{2}[2H \tan(\theta_s) - W_b]\Pi_c^{-1}P_1(X, T)\right), \quad (\text{C17})$$

where P_1 must be negative ($P_1 < 0$), so that

$$0 = \arccos(0) \leq \arccos\left(\frac{1}{2}[2H \tan(\theta_s) - W_b]\Pi_c^{-1}P_1\right) \leq \arccos(1) = \pi/2,$$

which is needed, since by Eq. (C14c), it follows that

$$\theta_s < \theta_f(x, t) = \theta_s + \frac{\pi}{2} - \frac{\theta_o(x, t)}{2} < \theta_s + \frac{\pi}{2}.$$

In the unpinned contact line case, the inclination angle is negative, namely, $\theta_s < 0$, and since W should satisfy $W > W_b$, we get instead the constraints in Eq. (34), the following ones: if $0 < (\theta_{f,A/R} - \theta_s) < \pi/2$, then $P_1(X, T)$ must be negative and satisfy

$$\Pi_c^{-1}P_1(X, T) > -\frac{2 \cos(\theta_{f,A/R} - \theta_s)}{W_b}. \quad (\text{C18a})$$

Otherwise, if $\pi/2 \leq (\theta_{f,A/R} - \theta_s) < \pi$, then $P_1(X, T)$ must be positive and satisfy

$$\Pi_c^{-1}P_1(X, T) < -\frac{2 \cos(\theta_{f,A/R} - \theta_s)}{W_b}. \quad (\text{C18b})$$

The rest remains the same as in the hydrophobic case.

APPENDIX D: NUMERICAL PROCEDURE

In this section we shall combine our results in Secs. II and III, and discuss our methodology of solution for the resulting system of equations inside the tube, $X \in [0, 1]$, in two cases. More specifically, let us consider the system of equations obtained by combining Eq. (15) and either Eq. (30) or Eq. (35) in the pinned or unpinned contact line limit, respectively. That is, we solve numerically the following nonlinear system:

$$\frac{1}{K} \frac{\partial^2 P_1}{\partial T^2} - \frac{\partial^2 P_1}{\partial X^2} = -\frac{\partial^2 A_1}{\partial T^2}, \quad (X, T) \in (0, 1) \times (0, T_{\text{final}}), \quad (\text{D1})$$

where T_{final} denotes some final time, and A_1 is given by either

$$A_1(P_1) = \frac{2W_b H - 2H^2 \tan(\theta_s)}{(1+n_g)W_b} + \frac{1}{(1+n_g)W_b \Pi_c^{-2}P_1^2} \times \left[2 \arccos \left\{ \left[H \tan(\theta_s) - \frac{W_b}{2} \right] \Pi_c^{-1}P_1 \right\} - \pi + \sin \left(2 \arccos \left\{ \left[H \tan(\theta_s) - \frac{W_b}{2} \right] \Pi_c^{-1}P_1 \right\} \right) \right] \quad (\text{D2})$$

or

$$A_1(P_1) = \frac{1}{2(1+n_g)W_b \tan(\theta_s)} \left[W_b^2 - \frac{4 \cos^2(\theta_{f,A/R} - \theta_s)}{\Pi_c^{-2} P_1^2} \right] + \frac{\left(2(\theta_{f,A/R} - \theta_s) - \pi + \sin \left\{ 2[\theta_{f,A/R} - \theta_s] \right\} \right)}{(1+n_g)W_b \Pi_c^{-2} P_1^2}. \quad (\text{D3})$$

We solve this system subject to two sets of supplementary conditions, as is detailed below.

Case 1: In this case we assume that the supplementary conditions are given by

$$\begin{aligned} P_1(X=0, T) &= \mathcal{A} \sin(\omega T), & T \in (0, T_{\text{final}}), \\ P_1(X=1, T) &= 0, & T \in (0, T_{\text{final}}), \\ P_1(X, T=0) &= \frac{\partial P_1}{\partial T} \Big|_{T=0} = 0, & X \in [0, 1]. \end{aligned} \quad (\text{D4})$$

Case 2: In this case we assume that the supplementary conditions are given by

$$\begin{aligned} P_1(X=0, T) &= \mathcal{B} \text{Heaviside}(T), & T \in (0, T_{\text{final}}), \\ \frac{\partial P_1}{\partial X} \Big|_{X=1} &= 0, & T \in (0, T_{\text{final}}), \\ P_1(X, T=0) &= \frac{\partial P_1}{\partial T} \Big|_{T=0} = 0, & X \in [0, 1], \end{aligned} \quad (\text{D5})$$

where we use the following smooth approximation for the Heaviside function:

$$\text{Heaviside}(T) := \frac{1}{1 + \exp[-k(T - 0.2)]},$$

where $k > 1$ is some fixed constant (in our runs we set $k = 7$).

We discretize our domain by an equi-spaced (with increment size ΔX) grid containing I nodes, which is regular near $X = 0$ and either regular (in Case 1) or staggered with a ghost point near $X = 1$, which is a convenient method when imposing Neumann boundary conditions; see, e.g., [45,46] (in Case 2). Further, we discretize time with N time levels and time step size ΔT . Thus, in each time level we solve $2I$ equations with $2I$ unknowns, $P_{1,1}^n, \dots, P_{1,I}^n, A_{1,1}^n, \dots, A_{1,I}^n$, where we use the following notation:

$$P_{1,i}^n = P_1(i\Delta X, n\Delta T).$$

Equation (D1) is discretized up through order $O(\Delta X^2, \Delta T^2)$, using the Crank-Nicolson scheme [47], so that at interior points ($i = 2, \dots, I - 1$) it yields the following equations:

$$\begin{aligned} \frac{1}{K} \frac{P_{1,i}^{n+1} - 2P_{1,i}^n + P_{1,i}^{n-1}}{\Delta T^2} - \frac{1}{2\Delta X^2} \left[(P_{1,i+1}^{n+1} - 2P_{1,i}^{n+1} + P_{1,i-1}^{n+1}) + (P_{1,i+1}^n - 2P_{1,i}^n + P_{1,i-1}^n) \right] \\ = - \frac{A_{1,i}^{n+1} - 2A_{1,i}^n + A_{1,i}^{n-1}}{\Delta T^2}. \end{aligned} \quad (\text{D6})$$

Equation (D6) at $i = 1, I$, is modified to take into account the boundary conditions near $X = 0$ and $X = 1$ in the appropriate manner. This allows us to fill in the first I rows of the mass matrix and the forcing term vector, which is based on the solution from the previous time level.

The nonlinear algebraic in Eqs. (D2) or (D3) can be linearized in the following manner. Let us assume that in a general case there exists a function G , which is determined according to Eqs. (D2)

or (D3), such that

$$A_1(P_1) = G(P_1). \quad (\text{D7})$$

If we assume that the time step is sufficiently small, so that $0 < \Delta P_{1,i} := P_{1,i}^{n+1} - P_{1,i}^n \ll 1$ for all nodes $i = 1, \dots, I$, then for all $i = 1, \dots, I$ we may expand the expression in Eq. (D7) in $\Delta P_{1,i}$ around $P_{1,i}^n$ up through order $O(\Delta P_{1,i}^2)$, as follows:

$$\begin{aligned} A_{1,i}^{n+1} &= G(P_{1,i}^n + \Delta P_{1,i}) \\ &= G(P_{1,i}^n) + \Delta P_{1,i} G'(P_{1,i}^n) + O(\Delta P_{1,i}^2) \\ &= A_{1,i}^n + \Delta P_{1,i} G'(P_{1,i}^n) + O(\Delta P_{1,i}^2), \end{aligned} \quad (\text{D8})$$

where $G'(P_{1,i}^n) := dG/dP_{1,i}^n$. This yields the following I equations:

$$A_{1,i}^{n+1} - G'(P_{1,i}^n) P_{1,i}^{n+1} = A_{1,i}^n - G'(P_{1,i}^n) P_{1,i}^n, \quad (\text{D9})$$

which allows us to fill the missing rows, $i = I + 1, \dots, 2I$, of the mass matrix and the forcing term vector.

The main obstacle in this procedure, which is otherwise straightforward, is to determine the correct form for G' , which is a discontinuous function at the corners of each hysteresis cycle (see Fig. 6). In order to get convergence in time, we need to smooth G' . Let us discuss our way to achieve this smoothing. Note that in all our simulations we start in the pinned mode, so for $n \leq 2$ we calculate G' based on differentiating Eq. (D2) with respect to P_1 . Thus, let us assume that $n > 2$. First, knowing the value of $P_{1,i}^n$ we calculate the contact angles, according to

$$\theta_{f,i}^n = \theta_s + \arccos\left(\frac{1}{2}[2H_i^n \tan(\theta_s) - W_b]\Pi_c^{-1} P_{1,i}^n\right), \quad (\text{D10})$$

for $i = 1, \dots, I$, and irrespective if $\theta_{f,R} < \theta_{f,i}^n < \theta_{f,A}$ or $\theta_{f,i}^n \geq \theta_{f,A}$ or $\theta_{f,i}^n \leq \theta_{f,R}$ for all $i = 1, \dots, I$, we calculate the corresponding functions:

$$\begin{aligned} G'_{i,\text{pinned}} &:= G'(P_{1,i}^n), && \text{by differentiating (D2),} \\ G'_{i,\text{unpinned-A}} &:= G'(P_{1,i}^n, \theta_{f,A}), && \text{by differentiating (D3),} \\ G'_{i,\text{unpinned-R}} &:= G'(P_{1,i}^n, \theta_{f,R}), && \text{by differentiating (D3).} \end{aligned} \quad (\text{D11})$$

Further, for all $i = 1, \dots, I$, we calculate the following smooth approximations to step and Heaviside functions:

$$\begin{aligned} \chi_{\text{pinned},i} &:= \frac{1}{1 + \exp[m(\theta_{f,i} - \theta_{f,A})]} + \frac{1}{1 + \exp[m(\theta_{f,R} - \theta_{f,i})]} - 1, \\ \chi_{A,i} &:= \frac{1}{1 + \exp[m(\theta_{f,A} - \theta_{f,i})]}, \\ \chi_{R,i} &:= \frac{1}{1 + \exp[m(\theta_{f,i} - \theta_{f,R})]}, \end{aligned} \quad (\text{D12})$$

where $m \geq 1$ is some fixed parameter prescribed by the user. In our simulations we set $m = 20$, but it appears that our simulations are not sensitive to the specific value of m . Note that

$$\chi_{\text{pinned},i} = \begin{cases} 1, & \text{if } \theta_{f,R} < \theta_{f,i}^n < \theta_{f,A}, \\ 0, & \text{if } \theta_{f,i}^n > \theta_{f,A} \text{ or } \theta_{f,i}^n < \theta_{f,R}, \end{cases} \quad (\text{D13})$$

and smoothly increases/decreases between 0 and 1. Further,

$$\chi_{A,i} = \begin{cases} 1, & \text{if } \theta_{f,i}^n > \theta_{f,A}, \\ 0, & \text{if } \theta_{f,i}^n < \theta_{f,A}, \end{cases} \quad (\text{D14})$$

and

$$\chi_{R,i} = \begin{cases} 1, & \text{if } \theta_{f,i}^n < \theta_{f,R}, \\ 0, & \text{if } \theta_{f,i}^n > \theta_{f,R}. \end{cases} \quad (\text{D15})$$

In other words, χ_{pinned} , χ_A , and χ_R are indicators, which indicate the mode of contact line motion: pinned, advancing, and receding, respectively.

Next, in order to verify if an advancing or a receding mode of motion of node i should be interchanged by the pinned mode, we define ΔH_i^n in the following manner:

$$\Delta H_i^n := \begin{cases} 0, & \text{if } \theta_{f,R} < \theta_{f,i}^n < \theta_{f,A}, \\ H_i^n - H_i^{n-1}, & \text{if } \theta_{f,i}^n \geq \theta_{f,A} \text{ or } \theta_{f,i}^n \leq \theta_{f,R}, \end{cases} \quad (\text{D16})$$

where at each time step, n , we set H_i^{n-1} to be the previous position of the contact line, and then modify H_i^n according to

(1) if $\theta_{f,i}^n \geq \theta_{f,A}$,

$$H_i^n = \frac{1}{2 \tan(\theta_s)} \left[W_b + \frac{2 \cos(\theta_{f,A} - \theta_s)}{\Pi_c^{-1} P_{1,i}^n} \right], \quad (\text{D17})$$

(2) if $\theta_{f,i}^n \leq \theta_{f,R}$,

$$H_i^n = \frac{1}{2 \tan(\theta_s)} \left[W_b + \frac{2 \cos(\theta_{f,R} - \theta_s)}{\Pi_c^{-1} P_{1,i}^n} \right]. \quad (\text{D18})$$

Now we define two additional (smoothed) Heaviside functions:

$$\begin{aligned} \chi_{\Delta H,A,i} &:= \frac{1}{1 + \exp(-m \Delta H_i^n)}, \\ \chi_{\Delta H,R,i} &:= \frac{1}{1 + \exp(m \Delta H_i^n)}. \end{aligned} \quad (\text{D19})$$

Note that

$$\chi_{\Delta H,A,i} = \begin{cases} 1, & \text{if } \Delta H_i^n > 0, \\ 0, & \text{if } \Delta H_i^n < 0, \end{cases}$$

and thus it indicates if node i should be in advancing mode of motion or not. Similarly,

$$\chi_{\Delta H,R,i} = \begin{cases} 1, & \text{if } \Delta H_i^n < 0, \\ 0, & \text{if } \Delta H_i^n > 0 \end{cases}$$

indicates if node i should be in receding mode of motion or not.

Finally, we define a smooth version of G' by using the definitions in Eqs. (D11), (D12), and (D19), as follows:

$$\begin{aligned} (G')_i^n &:= G'_{i,\text{pinned}} \chi_{\text{pinned},i} + G'_{i,\text{unpinned-A}} \chi_{A,i} \chi_{\Delta H,A,i} \\ &\quad + G'_{i,\text{unpinned-R}} \chi_{R,i} \chi_{\Delta H,R,i}, \quad i = 1, \dots, I. \end{aligned} \quad (\text{D20})$$

Note that if the various χ_i 's appearing in Eq. (D20), were the corresponding Heaviside and step functions (without any smoothing), then the expression in Eq. (D20) should constitute $G'(P_{1,i}^n)$

in accordance with the corresponding mode of motion of node i (in all possible cases). Hence, smoothing of χ_i 's actually implies that G' is determined according to the appropriate mode of motion for nodes whose mode of motion is far from the corners of the corresponding hysteresis cycle, and it is a smoothed sum of the derivatives which have a mutual corner on the corresponding hysteresis cycle for nodes whose mode of motion is in the proximity of a corner.

When $(G')_i^n$ is calculated for $i = 1, \dots, I$, according to Eq. (D20), we use it in Eq. (D9), solve the linear system of equations for P_1^{n+1} and A_1^{n+1} , and move to the next time step.

-
- [1] A. S. Tijsseling, A. Anderson, A. Isebree Moens, and D. J. Korteweg, On the speed of propagation of waves in elastic tubes, in *Proceedings of the 11th International Conference on Pressure Surges*, edited by S. Anderson (BHR Group, Lisbon, 2012), pp. 227–245.
- [2] G. Wertheim, *Mémoire Sur La Vitesse Du Son Dans Les Liquides* (Bachelier, 1848).
- [3] E. H. Barton, *A Text-book on Sound* (Macmillan, New York, 1922).
- [4] D. J. Korteweg, On the velocity of propagating sound in elastic tubes, *Ann. Phys.* **174**, 525 (1878).
- [5] A. Noordergraaf, Hemodynamics, in *Biological Engineering*, edited by H. P. Schwan. With contributions by Richard FitzHugh (McGraw-Hill, New York, 1969), pp. 391–545.
- [6] T. Fukui, K. H. Parker, and T. Yamaguchi, Pulse wave propagation in large blood vessels based on fluid-solid interactions methods, in *Single and Two-Phase Flows on Chemical and Biomedical Engineering*, edited by R. Dias, R. Lima, A. A. Martins, and T. M. Mata (Bentham Science Publishers Ltd, Bentham, 2012), p. 460.
- [7] H. Elkenani, E. Al-Bahkali, and M. Souli, Numerical investigation of pulse wave propagation in arteries using fluid structure interaction capabilities, *Comput. Math. Methods Med.* **2017**, 4198095 (2017).
- [8] J. Li, J. Melbin, R. Riffle, and A. Noordergraaf, Pulse wave propagation, *Circ. Res.* **49**, 442 (1981).
- [9] J. S. Lillie, A. S. Liberson, and D. A. Borkholder, Quantification of hemodynamic pulse wave velocity based on a thick wall multi-layer model for blood vessels, *J. Fluid Flow Heat Mass Transfer (JFFHMT)* **3**, 54 (2016).
- [10] D. Quéré, Wetting and roughness, *Annu. Rev. Mater. Res.* **38**, 71 (2008).
- [11] Y. Xue, P. Lv, H. Lin, and H. Duan, Underwater superhydrophobicity: Stability, design and regulation, and applications, *Appl. Mech. Rev.* **68**, 030803 (2016).
- [12] E. Lauga and H. O. Stone, Effective slip in pressure-driven stokes flow, *J. Fluid Mech.* **489**, 55 (2003).
- [13] J. Ou, B. Perot, and J. P. Rothstein, Laminar drag reduction in microchannels using ultrahydrophobic surfaces, *Phys. Fluids* **16**, 4635 (2004).
- [14] J. Ou and J. P. Rothstein, Direct velocity measurements of the flow past drag-reducing ultrahydrophobic surfaces, *Phys. Fluids* **17**, 103606 (2005).
- [15] C.-H. Choi and C.-J. Kim, Large Slip of Aqueous Liquid Flow over a Nanoengineered Superhydrophobic Surface, *Phys. Rev. Lett.* **96**, 066001 (2006).
- [16] R. Truesdell, A. Mammoli, P. Vorobieff, F. van Swol, and C. J. Brinker, Drag Reduction on a Patterned Superhydrophobic Surface, *Phys. Rev. Lett.* **97**, 044504 (2006).
- [17] J. Hyväluoma and J. Harting, Slip Flow Over Structured Surfaces with Entrapped Microbubbles, *Phys. Rev. Lett.* **100**, 246001 (2008).
- [18] P. Joseph, C. Cottin-Bizonne, J.-M. Benoît, C. Ybert, C. Journet, P. Tabeling, and L. Bocquet, Slippage of Water Past Superhydrophobic Carbon Nanotube Forests in Microchannels, *Phys. Rev. Lett.* **97**, 156104 (2006).
- [19] O. Schnitzer, Singular effective slip length for longitudinal flow over a dense bubble mattress, *Phys. Rev. Fluids* **1**, 052101(R) (2016).
- [20] O. Schnitzer and E. Yariv, Stokes resistance of a solid cylinder near a superhydrophobic surface. Part 1. Grooves perpendicular to cylinder axis, *J. Fluid Mech.* **868**, 212 (2019).
- [21] O. Schnitzer, R. Brandão, and E. Yariv, Acoustics of bubbles trapped in microgrooves: From isolated subwavelength resonators to superhydrophobic metasurfaces, *Phys. Rev. B* **99**, 195155 (2019).
- [22] D. G. Crowdy, Superhydrophobic annular pipes: A theoretical study, *J. Fluid Mech.* **906**, A15 (2021).

- [23] M. Sbragaglia and A. Prosperetti, A note on the effective slip properties for microchannel flows with ultrahydrophobic surfaces, *Phys. Fluids* **19**, 043603 (2007).
- [24] L. Lei, H. Li, J. Shi, and Y. Chen, Diffraction patterns of a water-submerged superhydrophobic grating under pressure, *Langmuir* **26**, 3666 (2010).
- [25] S. E. Game, M. Hodes, and D. T. Papageorgiou, Effects of slowly-varying meniscus curvature on internal flows in the Cassie state, *J. Fluid Mech.* **872**, 272 (2019).
- [26] S. Dehe, B. Rofman, M. Bercovici, and S. Hardt, Electro-osmotic flow enhancement over superhydrophobic surfaces, *Phys. Rev. Fluids* **5**, 053701 (2020).
- [27] M. Perlin and W. W. Schultz, Capillary effects on surface waves, *Annu. Rev. Fluid Mech.* **32**, 241 (2000).
- [28] J. Miles, The capillary boundary layer for standing waves, *J. Fluid Mech.* **222**, 197 (1991).
- [29] D. M. Henderson and J. W. Miles, Surface-wave damping in a circular cylinder with a fixed contact line, *J. Fluid Mech.* **275**, 285 (1994).
- [30] S. T. Milner, Square patterns and secondary instabilities in driven capillary waves, *J. Fluid Mech.* **225**, 81 (1991).
- [31] B. Christiansen, P. Alstrom, and M. T. Levinsen, Dissipation and ordering in capillary waves at high aspect ratios, *J. Fluid Mech.* **291**, 323 (1995).
- [32] L. Jiang, C.-L. Ting, M. Perlin, and W. W. Schultz, Moderate and steep Faraday waves: Instabilities, modulation and temporal asymmetries, *J. Fluid Mech.* **329**, 275 (1996).
- [33] A. Gat, H. Navaz, and M. Gharib, Dynamics of freely moving plates connected by a shallow liquid bridge, *Phys. Fluids* **23**, 097101 (2011).
- [34] J. Shelton and P. H. Trinh, Exponential asymptotics for steady parasitic capillary ripples on steep gravity waves, *J. Fluid Mech.* **939**, A17 (2022).
- [35] M. K. Tan, J. R. Friend, O. K. Matar, and L. Y. Yeo, Capillary wave motion excited by high frequency surface acoustic waves, *Phys. Fluids* **22**, 112112 (2010).
- [36] M. L. Douvidzon, S. Maayani, L. L. Martin, and T. Carmon, Light and capillary waves propagation in water fibers, *Sci. Rep.* **7**, 16633 (2017).
- [37] S. Ly, G. Guss, A. M. Rubenchik, W. J. Keller, N. Shen, R. A. Negres, and J. Bude, Resonance excitation of surface capillary waves to enhance material removal for laser material processing, *Sci. Rep.* **9**, 8152 (2019).
- [38] H. Rathgen, K. Sugiyama, C.-D. Ohl, D. Lohse, and F. Mugele, Nanometer-Resolved Collective Micromeniscus Oscillations through Optical Diffraction, *Phys. Rev. Lett.* **99**, 214501 (2007).
- [39] H. Rathgen and F. Mugele, Diffraction patterns of a water-submerged superhydrophobic grating under pressure, *Faraday Discuss.* **146**, 49 (2010).
- [40] J. D. Anderson, *Modern Compressible Flow: With Historical Perspective*, 2nd ed. (McGraw-Hill, New York, 1990).
- [41] A. Ferrari, Exact solutions for quasi-one-dimensional compressible viscous flows in conical nozzles, *J. Fluid Mech.* **915**, A1 (2021).
- [42] A. Bermúdez, X. López, and M. E. Vázquez-Cendón, Finite volume methods for multi-component Euler equations with source terms, *Comput. Fluids* **156**, 113 (2017).
- [43] P.-G. de Gennes, F. Brochard-Wyart, and D. Quere, *Capillarity and Wetting Phenomena: Drops, Bubbles, Pearls, Waves* (Springer-Verlag, New-York, 2004).
- [44] See Supplemental Material at <http://link.aps.org/supplemental/10.1103/PhysRevFluids.7.064803> for a movie which contains three short movies extracted from our simulations which visualize the dynamics of the pressure, the film thickness, and the contact angle. These movies correspond to Cases 1 and 2 (Figs. 6–8 in the paper) in the paper and provide an additional example of a simulation in Case 1 with a much larger sinusoidal signal frequency in the inlet, than it was shown in Fig. 6.
- [45] J. Arteaga-Arispe and J. M. Guevara-Jordan, A conservative finite difference scheme for static diffusion equation, *Divulgaciones Matemáticas* **16**, 39 (2008).
- [46] M. Shashkov, *Conservative Finite-Difference Methods on General Grids* (CRC Press, Boca Raton, FL, 1996).
- [47] J. Crank and P. Nicolson, A practical method for numerical evaluation of solutions of partial differential equations of the heat-conduction type, *Math. Proc. Cambridge Philos. Soc.* **43**, 50 (1947).